PECVD GROWTH OF Si_x:Ge_{1-x} FILMS FOR HIGH SPEED DEVICES AND MEMS

by

Srinivasan Kannan

A thesis submitted to the graduate school of
University of Utah
In partial fulfillment of the requirements for the degree of

Master of Science

Department of Physics

The University of Utah

July 2005

Copyright © Srinivasan Kannan 2005

All Rights Reserved

Knowledge is serene and indestructible wealth;
there is nothing else in benefits to compare
- Thiruvalluvar

Dedicated to my loving parents, sister and loyal friends

ABSTRACT

PECVD growth of Si_x:Ge_{1-x} films for high speed devices and MEMS

SiGe thin films were deposited by plasma enhanced chemical vapor deposition (PECVD; MV Systems, Colorado) for use in high speed devices, Micro-Electrical Mechanical Systems (MEMS) and measurement of electromagnetic radiation (bolomtery). SiGe films grown by PECVD typically have lower stress, lower deposition temperatures and high growth rate (200 Å/min) compared with other deposition techniques. Increasing the germane concentration in the vapor phase allows the deposition temperature to be decreased, which decreases the thermal conductivity of the samples and improves their properties for bolometry. Films with lower germanium concentration are smoother. The samples were deposited at temperatures from 500 ^{o}C to 580 ^{o}C and doped using either diborane (B_2H_6) or phosphine (PH_3). As-deposited films had predominantly (111) texture and some (110) texture as determined by X-ray diffraction. Annealing produced crystalline material with no evidence of cracking as determined by resistivity measurements. Annealing produces a variation of crystallite orientation with predominantly (111) texture. As-grown, boron doped samples have resistivities varying from 1.3 mO-cm to 44 mO-cm depending upon germanium concentration (100% to 20%). As-grown phosphorous doped samples (T_s = 580 ^{o}C) with Ge concentration at 30% had higher resistivity of ~ 5.1 O-cm. As-grown films had stresses as low as 18 MPa tensile. Stress in annealed samples varied with annealing temperature and time. An increase in annealing temperature increased stress in the films. For samples with low germanium concentration; Fourier transform infrared spectroscopy (FTIR) was used to

identify the chemical bonding in the sample. Energy Dispersive X-Ray analysis (EDX) provided alloy compositions, which were verified by X-ray diffraction calculations. Photothermal Deflection Spectroscopy (PDS) was used to determine optical band gaps. SiGe is good for high speed devices and MEMS applications because of low as-grown stress and low resistivity in the samples.

TABLE OF CONTENTS

	PAGE
ABSTRACT	
LIST OF TABLES	
LIST OF FIGURES	
ACKNOWLEDGEMENT	
CHAPTER	
1.0 INTRODUCTION	1
1.1 Historical Background	1
1.2 Motivation	1
1.3 Objective	5
2.0 BACKGROUND	6
2.1 Silicon and Germanium: properties	6
2.2 Growth conditions	7
2.3 Stress Measurements	7
2.4 Annealing & Grain size	8
2.5 Resistivity	8
2.6 X-Ray Diffraction	9
2.7 Fourier Transform Infrared Spectroscopy	10
3.0 EXPERIMENTAL APPROACH	11
4.0 CHARACTERIZATION TOOLS	13
4.1 PECVD reactor tool	13
4.2 Energy Dispersive X-Ray Analysis(EDX)	16
4.3 X-Ray Diffraction (XRD)	17
4.4 Profilometry: Stress Measurements	19
4.5 Fourier Transform Infrared Spectroscopy	20
4.6 Four Point Probe Measurements	22
4.7 Photothermal Deflection Spectroscopy (PDS)	24
4.8 Atomic Force Microscopy	26

5.0 RESULTS 28

5.1 Growth Conditions 28
5.2 Energy Dispersive X-Ray Analysis (EDX) 28
5.3 X-Ray Diffraction (XRD) 30
5.4 Stress Measurements 33
5.5 Fourier Transform Infrared Spectroscopy (FTIR) 39
5.6 Surface texture 42
5.7 Resistivity Measurements 43
5.8 Photothermal Deflection Spectroscopy (PDS) 46

6.0 DISCUSSION 49

6.1 Growth conditions & EDX 49
6.2 X-Ray Diffraction 50
6.3 Stress Measurements 52
6.4 Fourier Transform Infrared Spectroscopy 53
6.5 Surface texture 54
6.6 Resistivity Measurements 54
6.7 Photothermal Deflection Spectroscopy(PDS) 55

7.0 SUMMARY / FUTURE WORK 57

APPENDIX 60

LIST OF REFERENCES 72

List of Tables

Table		Page
5.1	X-Ray Diffraction data for as grown SiGe phosphorous doped sample.	30
5.2	X-Ray Diffraction data for annealed sample	31
5.3	Effect of deposition parameters on stress variation in SiGe samples	33
5.4	Stress data for annealed samples with different germanium concentrations.	34
5.5	Resistivity values for boron doped SiGe alloy for different germanium concentrations.	43
5.6	Resistivity values for phosphorous doped SiGe alloy for different germanium concentration.	43
6.1	X-Ray Diffraction data for as grown sample showing higher Germanium concentration.	51
8.1	X-Ray Diffraction data for as grown SiGe phosphorous doped sample.	60
8.2	X-Ray Diffraction data for as grown SiGe boron doped sample.	60
8.3	X-Ray Diffraction data for as grown SiGe phosphorous doped sample.	60
8.4	X-Ray Diffraction data for as grown SiGe phosphorous doped sample.	61
8.5	X-Ray Diffraction data for as grown SiGe boron doped sample.	61
8.6	X-Ray Diffraction data for phosphorous doped annealed sample	64
8.7	X-Ray Diffraction data for phosphorous doped annealed sample	64

Table	**Page**
8.8 X-Ray Diffraction data for boron doped annealed sample	65
8.9 Comparison of Silicon, Germanium and SiGe properties	70

List of figures:

Figure No		Page
4.1	Schematic diagram of PECVD system	15
4.2	Principle of Energy Dispersive X-Ray analysis	16
4.3	(110) Orientation in a unit cell	18
4.4	X-Ray diffraction setup and principle	18
4.5	Michelson Interferometer principle	20
4.6	Block Diagram of FTIR.	21
4.5	Principle and setup of four point probe measurement	23
4.6	Principle behind Photothermal Defelction Spectroscopy	26
5.1	Data showing EDX Analysis spectrum	29
5.2	Data showing X-Ray diffraction peaks for as grown phosphorous doped sample	32
5.3	Data showing X-Ray Diffraction peaks for phosphorous doped annealed sample.	32
5.4	Data showing variation of stress with germanium concentration	35
5.5	Effect on annealing temperature on stress for fixed germanium concentration	36
5.6	Stress variation with anneal temperature	37
5.7	Stress variation with thickness	38
5.8	FT-IR spectra showing convoluted Si-H and Ge-H peaks	39
5.9	FT-IR spectra showing absence of Si-H and Ge-H in annealed sample	40
5.10	FT-IR spectra showing convoluted Si-H and Ge-H peaks	41
5.11	Surface texture for annealed boron doped sample	42

Figure No **Page**

5.12 Surface texture for as grown boron doped sample 42

5.13 Surface texture for annealed phosphorous doped sample 42

5.14 Surface texture for as grown boron doped sample 42

5.15 Resistivity for as grown boron doped samples 44

5.16 Resistivity for annealed boron doped samples 45

5.17 Resistivity for as grown phsophorous doped samples 45

5.18 Resistivity as a variation of anneal temperatures 46

5.19 PDS spectra showing sub band gap absorption and band gap 47

5.20 PDS spectra showing absorption for annealed and as grown sample 48

7.1 PECVD poly-SiGe as encapsulating layer above a Bosch accelerometer and HF etching of sacrificial SiO_2 59

8.1 Data showing X-Ray diffraction peaks for as grown phosphorous doped sample 61

8.2 Data showing X-Ray diffraction peaks for as grown phosphorous doped sample 62

8.3 Data showing X-Ray diffraction peaks for as grown boron doped sample 62

8.4 Data showing X-Ray diffraction peaks for as grown boron doped sample 63

8.5 Data showing X-Ray diffraction peaks for as grown boron doped sample 63

8.6 Data showing X-Ray Diffraction peaks for phosphorous doped annealed sample. 65

8.7 Data showing X-Ray Diffraction peaks for phosphorous doped annealed sample. 66

8.8 Data showing X-Ray Diffraction peaks for boron doped annealed sample. 66

<u>Figure No</u> **Page**

8.9 Curvature of substrate: 7059 glass 67

8.10 Curvature of substrate: as grown film 68

8.11 Curvature of substrate: annealed sample 69

ACKNOWLEDGEMENT

I am indebted to my thesis supervisors, Dr. Craig Taylor and Dr. David Allred for their expert guidance throughout the development of this project. Their guidance on the academic front helped me immensely in achieving my goals. I would also like to express my gratitude towards the Graduate school and Physics department for funding my academic expenses at the University of Utah.

I would like to specially thank Dr Craig Taylor for considering my request to join the group in summer of 2003. It was great experience learning about vacuum technology and appreciate Dr. Taylor for providing me an opportunity to do develop new skills. Dr. Allred with his hands on approach with respect to the project helped me immensely in understanding growth mechanisms of thin films.

I would like to acknowledge Matt DeLong and John Viner for offering to do chemical analysis and absorption measurements on the samples. Additionally, I express my gratitude towards Matt for upkeep of research facilities within the Physics department. I express my gratitude towards Dr Colin Inglefield for helping me with Atomic Force Microscopy (AFM) measurements.

I would like to thank Dr. Loren Rieth for his involvement in fruitful discussions with respect to vacuum technology and characterization techniques involved with the project. I

also would like to acknowledge Brian Baker and the rest of the microfab support staff for their willingness to help me overcome problems with the thin film deposition cluster tool.

The staff personnel at the physics department were very supportive during my stay and would like to appreciate them for helping run the day to day department administrative activities efficiently. My fellow peers in the group have been very supportive and I have enjoyed their company during my stint.

My parents, Mr. P.Kannan and Smt. Ranganayaki; have been supportive all these years and have been an inspiration throughout my career. What I have achieved, would not have been possible without their unending support. I would like to express my gratitude towards my sister and brother-in-law for their council in personal and professional life.

My friends, Saravana Kumar and Saravana Shankar have been highly supportive throughout my undergraduate and graduate study. I am indebted to them for their loyalty and appreciate their friendship. I would also like to thank the “Parkhavetis” for the great times I have spent with them during my undergraduate and graduate study. Special thanks to Sumona Banerjee and Bharathi Vedula for taking care of my “bhooking” concerns in the run up to my theses defense. Last but not the least, members of the “Pakao gang”; it would not have been possible to achieve my graduate degrees in electrical and physics without your “pakaos” to entertain me and keep me in good spirits.

1.0 INTRODUCTION:

1.1 Historical Background:

Even though the first transistors made were based on germanium (Ge), silicon (Si) has been the principal material driving semiconductor technology due to its larger bandgap and the better insulating properties of silicon-di-oxide (SiO_2). Silicon alloyed with germanium has a wide range of applications ranging from micro-electrical mechanical system (MEMS) structures to high speed electronics [11].

Silicon Germanium (SiGe) alloys have interested researchers and have been widely studied. There has been great interest in the influence of growth conditions on the electronic and structural properties of SiGe films [1]. SiGe offers a platform for post-processing of MEMS structures on top of prefabricated driving electronics, and this material is also a promising candidate for polycrystalline thin film transistors (TFTs) used in liquid crystal displays due to the ability to engineer bandgap [2]. SiGe also possesses good electrical and mechanical characteristics comparable with silicon.

1.2 Motivation: Post-processing of MEMS and High speed electronics

The semiconductor industry is dominated by silicon-based devices [3] due to its stable natural oxide which serves as an insulation and passivation layer. Silicon accounts for approximately 95% of sales in global semiconductor technology [3]. Its electrical, mechanical and chemical properties make it essential to the fabrication of billions of transistors making it ideal for high speed electronics. Silicon as a semiconductor is

restricted in terms of application in the field of optoelectronics due to its indirect band-gap. Many research efforts have concentrated on the development of alternative materials with improved high-frequency behavior and optoelectronic functionality.

Alternative technologies, such as III-V semiconductors, have superior optical and electrical characteristics compared to silicon, but the properties of SiO_2 and Si_3N_4 help provide superior insulating layers for transistors that reduce the leakage currents. III-V materials are faster compared to silicon based technologies, but in this era of low manufacturing cost and reduced leakage currents, silicon based technologies dominate the market. Silicon-based technologies are cheaper than III-V technologies and silicon-germanium (Si_xGe_{1-x}) has emerged as a material, which can be processed with silicon based technologies and deliver electrical performance on par with a III-V semiconductors. SiGe layers can be grown micro-crystalline at temperatures as low as 550 ºC. SiO_2 and Si_3N_4 also provide good insulating properties. SiGe has a current density of 10^6 A/cm^2 compared with 10^5 A/cm^2 for GaAs. Band gap engineering is also possible in the SiGe system by varying the germanium concentration in the alloy. Formerly, bandgap engineering has focused on III-V materials.

Complementary Metal Oxide Semiconductor (CMOS) technology remains the foundation of fundamental integrated circuit (IC) technology with gate lengths expected to decrease until the next decade (22nm by 2016) before problems with oxide layers take over. III-V materials exploit band offsets for confinement of carriers in a quantum well. The substantial lattice mismatch and anti-phase boundary (correct stacking but bond type is

wrong) formation incurred when growing III-V layers on Si make this combination highly unattractive to the semiconductor industry. III-V materials have been successful in light emitting diodes (LED) and field effect transistors [6]. The hope is to develop a new material compatible with existing silicon based technologies, which has properties superior to the existing Si technology [4,5,6,7].

With the transition between technology nodes becoming increasingly more difficult and expensive, Si CMOS is turning to SiGe for assistance. Intel and IBM have been highly successful in developing 45 nm technology nodes at the research level and this technology is moving towards production. A 45nm node is slated to go into production at the end of 2009(International technology roadmap for semiconductors).Among the new materials being considered for the 45 nm node are strained silicon, SiGe, high-k gate dielectrics , metal gates and germanium on insulator (GOI). It is expected that SiGe will make its way into optoelectronic and MEMS devices before 2010. IBM is already developing SiGe flip chip optical receivers with an eye on unlimited distance-bandwidth product.

SiGe also has potential application in MEMS. IMEC research institute in Belgium has successfully developed micro-system technologies based on SiGe. Post-CMOS integration of MEMS allows the use of conventional CMOS processes and a fairly independent optimization of the CMOS and MEMS processes. However, this procedure dictates a lower thermal budget for MEMS processing. Poly-SiGe provides properties required for MEMS applications at significantly lower temperatures (500°C) compared to

poly-Si (=800°C) [1]. A lattice mismatch of only 4% between Si and Ge results in less stress and thermal conductivity of SiGe layers is low making it ideal in MEMS applications.

Infineon demonstrated high speeds for frequency dividers and oscillators in SiGe:C bipolar process technology. Measured performances in these 100 GHz class components show 10 to 30% higher operating frequencies compared to competing circuits. Devices and products benefiting from these research results in the short term will be high-speed discretes for broadband networks and automotive radar transceivers. In MEMS, SiGe/Si/Cr bent cantilevers based on special epitaxial films have been made by S.V.Golod, D.Grutzmacher, C.David at Paul Scherrer Institute, Switzerland. There is a need for new technological methods allowing fabrication of nanocantilevers from thin multilayered structures. The method is called self-scrolling and is based on wet and dry etching of thick Molecular Beam Epitaxy (MBE) grown layers, which provides simplicity and reproducibility. This approach is compatible with standard silicon-based integration technology so it should be possible to produce sensitive high-frequency devices. [8]

Intel already has the 90 nm technology running on SiGe. IBM is reportedly working to have strained Si-on-insulator structures in production in about one year. SiGe has much to offer in solar cell and micro-electromechanical technology [9]. SiGe devices are matching III-V devices in terms of speed, and beating them on costs [10]

1.3 Objective:

Polycrystalline silicon (poly-Si) has been widely used in MEMS applications and high speed devices. The main disadvantage is the high deposition temperature (>800 ºC) required to grow poly-crystalline resulting in incompatibility with CMOS processes. Poly-crystalline SiGe is an excellent alternative having similar or better, properties with respect to MEMS applications (see Table 8.1).

The presence of germanium reduces the deposition temperature of the SiGe alloy allowing growth on low cost substrates and post processing of MEMS on top of CMOS process [11]. SiGe films for high speed devices and MEMS need low resistivity and low stress in the films .The thermal budget for the growth process also needs to be lower for bolometry, used to measure infared radiation.

X-ray diffraction and stress measurements were performed on the samples to characterize the structural properties of the films. Grain sizes, resistivity and bandgap engineering will also be studied by variation of growth conditions and germanium concentration. Previous research [11] has attributed cracking of the film to the release of hydrogen from the sample. Experiments on the variation of critical deposition parameters such as deposition temperature and pressure combined with characterization by Fourier transform infrared (FT-IR) spectroscopy will give an indication of the hydrogen present in the sample.

2.0 BACKGROUND

2.1 Silicon and germanium: properties

Silicon and germanium are the only group IV elements that form a continuous solid solution with gradually changing properties over the entire composition range [12]. The elements are randomly distributed in a diamond lattice, with the lattice parameter increasing nearly linearly with Ge content from a_{Si} = 5.431 ? to a_{Ge}= 5.658 ? [13]. The maximum lattice mismatch between Si and Ge is 4.2%. The fundamental bandgaps of Si and Ge are indirect, as are those for all SiGe alloys.

Carrier transport in semiconductors is usually expressed by the mobility of the career. The mobility(μ) is inversely proportional to the effective mass. Room-temperature electron and hole mobilities are significantly higher in Ge (μ_e= 3900 cm2 $V^{-1}s^{-1}$ and μ_h= 1800 cm2 $V^{-1}s^{-1}$) than in Si (μ_e=505 cm^2 $V^{-1}s^{-1}$ and μ_h= 1450 cm^2 $V^{-1}s^{-1}$) because of the smaller effective mass in Ge [14]. The hole mobility of pure Ge is higher than that of any III-V compound semiconductor.

Germanium reduces the melting point of SiGe alloys. For higher Ge concentrations, the alloy can be grown polycrystalline by PECVD at temperatures as low as 450 ºC. For as grown films, the crystallite orientations are predominantly in the (100) and (111) planes. Films deposited at lower plasma power are reported to have higher amorphous content. Poly SiGe is also proposed as a material for IR bolometers due to its low thermal conductivity compared to poly Si [11]. This material has a large temperature coefficient of resistivity (TCR) comparable to vanadium oxide which is used in bolometers [16]

2.2 Growth conditions:

PECVD grown poly SiGe has been proposed as a material which can be grown at a high deposition rate (upto 200 nm/min) and also possess excellent MEMS properties i.e Young's modulus, lattice mismatch, thermal conductivity) at low deposition temperatures. The deposition rate can be increased by increasing plasma power which may however degrade the structural properties of the material. At higher deposition rates, the amorphous-to-crystalline transition will occur at a higher temperature. The time at the deposition temperature is shorter than for a low-growth-rate process, and therefore the thermal budget is decreased. [16]

For the same germane and silane flow, poly Ge growth rates increase compared to poly Si indicating the deposition of Ge is reaction-rate limited. As the silane flow rates are increased and reactor pressure held constant, the partial pressure of germane decreases so that the probability of a Ge atom incorporating decreases.

2.3 Stress Measurements:

Stress plays a major role in device reliability and can cause films to peel off the substrate. Stress has been calculated by measuring the curvature of the substrate before and after deposition [11]. As deposited films have a low compressive stress for low Ge concentrations, and a high tensile stress is obtained if the layers are annealed at higher temperatures (= 525 ºC). At high temperatures cracks and pin holes are formed which were attributed to crystallization of films following the release of hydrogen [11].

Temperature also has a major effect on stress with increased annealing temperatures (> 550 ºC) and time (>4 hours) leading to increased tensile stress in the films. As grown films, which have compressive stress, are relieved by heating them in a furnace [17].

2.4 Annealing and grain size:

Tensile stress is preferred because free standing compressive films can buckle under compressive stress. Thermal annealing in a nitrogen atmosphere yields crystallization at temperatures = 550 ºC and also changes the stress to tensile [11]. Crystallization at higher temperatures produces films with lower resistvity but higher stress. Films can also crack at high temperatures. Pulsed laser annealing yields crystalline layers having a dominant (111) texture [21]. The crystallization depth using this technique is limited to 0.8µm leading to applications where it is possible to locally modify the physical features of the film without significantly affecting the underlying areas. Grain sizes in laser annealed samples are on the order of 340 nm [18].Grain sizes obtained by thermal annealing are on the order of 50 nm [19].

2.5 Resistivity:

As grown layers without plasma have lower resistivity while layers deposited by PECVD have a higher resistivity [11]. Layers deposited at lower temperature are amorphous and have high resistivity. To obtain *in-situ* polycrystalline layers with low resistivity, a higher deposition temperature is necessary. *In-situ* doping with boron results in resistivity values as low as 1 m? -cm [20]. For higher germanium concentrations, the resistivity values are lower (~ 1 m? -cm) for as grown samples. The resistivity of boron doped samples is

unaffected by an increase in annealing temperature while phosphorous-doped samples decreases noticeably due to dopant activation. Decreasing the Ge content below 70 % produces a significant increase in the resistvity for as grown material. The higher resistivity of phosphorous dopes samples is due to dopant segregation at the grain boundaries [20]. Boron doped films show a decreasing minimum sheet resistance (R_s) with increasing Ge fraction, while phosphorus doped films exhibit the reverse behavior. [16]

2.6 X-Ray Diffraction:

As grown SiGe layers have appreciable amorphous content for lower germanium concentrations. The texture of poly $Si_{11}Ge_{89}$ is much rougher than $Si_{31}Ge_{69}$ with sharp <220>, <331> and <331> x-ray scattering peaks. The <111> peak is broader and has higher intensity indicating the grains associated with higher Ge concentration are finer. Randomly orientation peaks result when boron doped samples are annealed at = 550 ºC for 30 minutes [1]. Increasing the germanium concentration shifts the peak to lower 2? positions due to change in lattice constant for different Ge concentrations. The shift is contributed to change in Ge concentration than due to stress in the films. The 2? position is shifted by 0.2º for a stress greater than 1.5 GPa [21].

2.7 Fourier Transform Infrared Spectroscopy (FT-IR):

The Fourier-transform infrared spectroscopy (FTIR) measures the content of bonded H and the silicon-hydrogen and germanium-hydrogen bonding configurations. In hydrogenated amorphous SiGe samples, two absorption peaks are observed near 640cm^{-1} and 2000 cm^{-1}, corresponding to the wagging and stretching modes of Si-H and Ge-H, respectively. The hydrogen content decreases in the samples grown with a decreased flow ratio of H_2 to GeH_4 + Si_2H_6 [22, 23]. The intensity of the wagging bands is proportional to the amount of hydrogen content in the sample. The hydrogen in the sample is bonded to both Si and Ge. At annealing temperatures up to 300 ºC, the wagging Ge-H_2 and Si-H_2 modes disappear but the stretching Ge-H and Si-H modes are still present. On annealing at 550 ºC, the stretching modes also totally disappear due to effusion of hydrogen from the sample.

3.0 EXPERIMENTAL APPROACH:

The major application of the material developed in this project is towards optical bolometers and to allow processing of MEMS structures on CMOS devices. Depositing poly-Si requires deposition temperatures as large as 800 ºC. Adding germanium reduces the deposition temperatures as low as 450 ºC depending upon the germanium concentration. Adding germanium results in a rougher sample surface, and more residual stress. High stress is not good for MEMS structures or for electronic devices. For bolometry, the thermal budget of the material should be smaller i.e the material being deposited should be exposed for a shorter time to the deposition temperature before deposition [11]. The deposition time should be short, without causing additional stress in the films.

Germanium concentration is high compared to silicon for similar flow rates of GeH_4 and SiH_4. The Ge concentration is kept at 20% to minimize surface roughness and the hydrogen concentration is minimized by depositing at higher temperatures. Hydrogen effusion on annealing tends to break the film [11].

The initial experiments used a 2:1 flow ratio between silane and germane to set the Ge concentrations. Chemical analysis by EDX provided feedback to change the flow rates to decrease or increase the germanium concentration.

Deposition temperatures were also high to incorporate less hydrogen in the alloy and to increase the growth rate [11]. Once high growth rates and germanium concentrations of roughly 20% were achieved, experiments were performed to test the effect of stress, thickness, deposition pressure and deposition temperature on the structural and electronic properties. Samples were also annealed to check for cracking due to hydrogen effusion from the sample upon heating. The effects of stress on the films will be discussed for the annealed films.

4.0 CHARACTERIZATION TOOLS:

4.1 PECVD reactor tool:

The three chamber Plasma enhanced chemical vapor deposition (PECVD) reactor was purchased from MV Systems, Golden, Colorado in January 1992. The system was rebuilt in 2003-2004 by replacing defective parts, rebuilding the chamber from scratch and enhancing the vacuum in the chamber. All connection, welds and assemblies were checked for leaks using a helium leak detector with 10^{-7} Torr rating.

Gas source system:

The gas cylinders are situated in an explosion proof stainless steel cabinet, which is continuously vented to the atmosphere. VLSI grade of silane, germane, phosphine and diborane were supplied for the project. The silane cylinder had a two stage regulator and a stainless steel cross-purging assembly to assure safety. The gas lines connecting the cylinders to the chamber had a manual shut off valve. All tube connections, welds and fittings were chosen to be VCR™ fittings. The mass-flow controller assemblies included a stainless steel manifold for gas mixing, an air- actuated valve and a purge line with a toggle valve.

High-temperature deposition chamber:

The PECVD chamber consisted of a horizontal, flat plate electrode 5” x 5”. The electrode (lower) was mounted on four adjustable length screws to control the distance between the sample holder and the electrode. The sample holder along with the rails formed the

second electrode (upper). The lower electrode was connected to a manual matching network and an RF generator through an RF feed-through. External ring heaters were mounted on the heater well and were connected to a temperature controller and a thermocouple. The heater well and chamber were sealed via a copper gasket. The heater well was removed whenever cleaning of the chamber was required. Two outlets for the baratron pressure gauge (10^{-3} Torr) and for an ion gauge (below 10^{-4} Torr). All exhaust gases from the PECVD is run through a burn box that will combust any gases that do not react in the chamber.

Vacuum pumps:

To maintain the chamber under high vacuum and drive out the effluent chamber gases, a Leybold mechanical vane pump and Varian turbo-molecular pump were employed. Prior to deposition, the operation of turbo-pump was necessary to ensure high vacuum in the chamber (10^{-7} Torr). During deposition, the deposition pressure is maintained using a throttle valve controlled by a MKS 600 series pressure controller. An automatic security valve and a molecular sieve trap were employed between the turbo pump and mechanical pump to prevent the vane pump oil from back streaming.

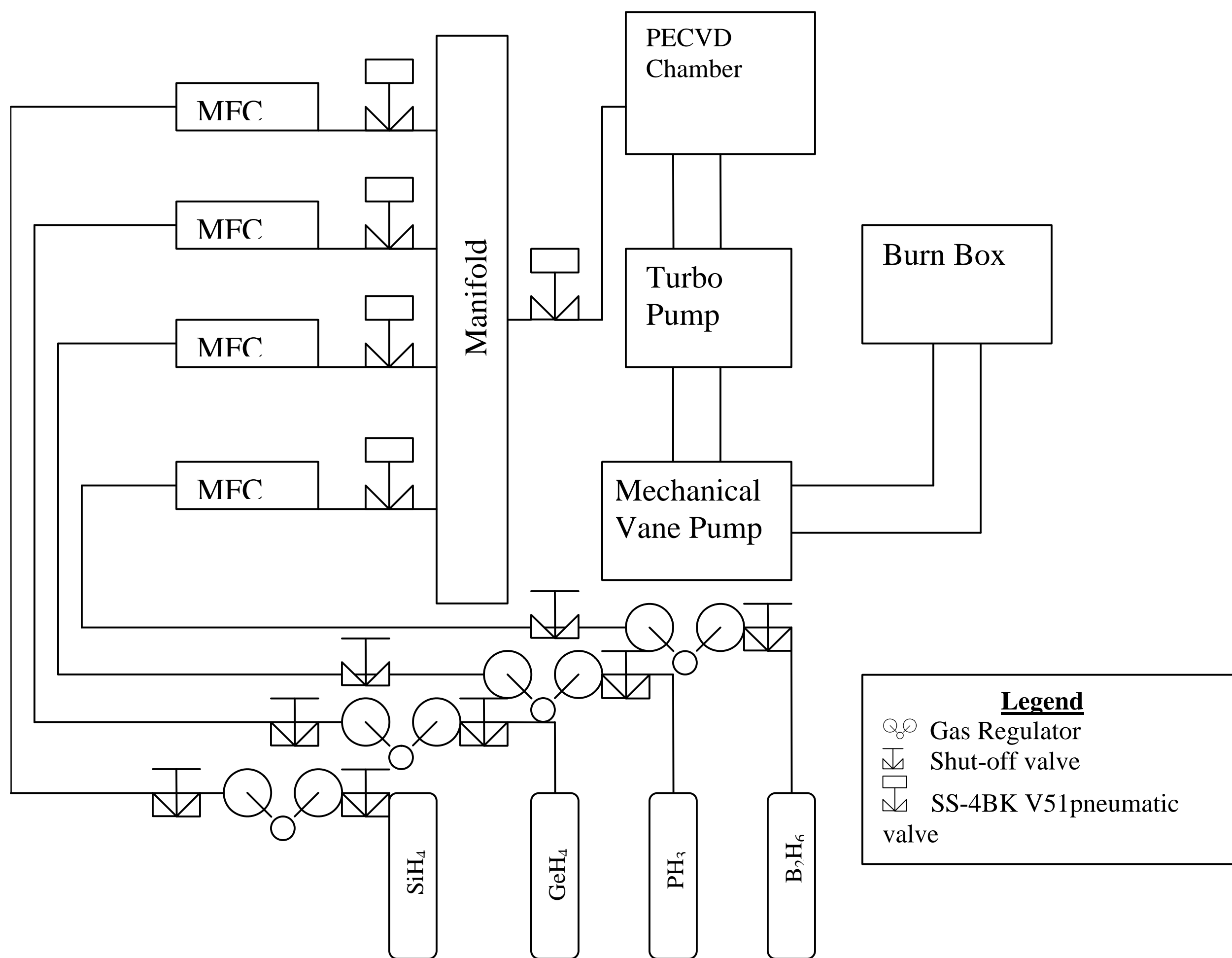

Figure 4.1 shows schematic diagram of PECVD system

4.2 Energy Dispersive X-Ray Analysis (EDX):

General Principle:

Interaction of accelerated electrons with sample produces a spectrum of X-rays. Electrons in the inner shells of the specimen atoms are excited by interaction with the electron beam. The outer orbital electrons fill the inner shell resulting in the production of X-ray photons, which have characteristic energies. Comparing the relative intensities of X-ray peaks can be used to determine the relative concentration of each element in the specimen except H_2, He and Li. Shown below is a figure depicting the principle behind EDX.

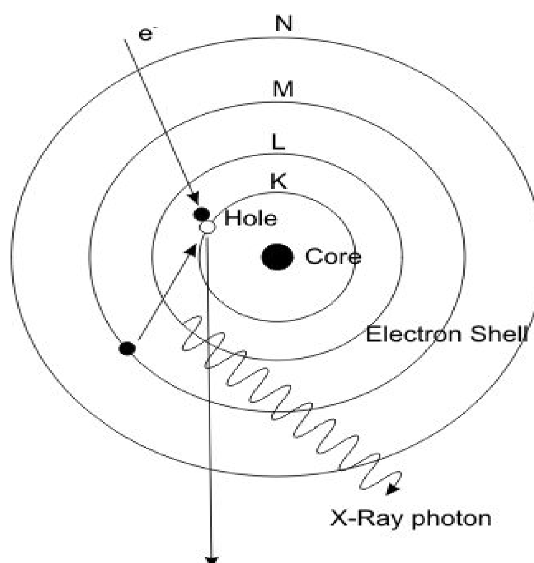

Figure 4.2 shows the principle behind EDX technique. (http://www.physik.uni-jena.de)

The basic assumption that underlies all quantitative x-ray microanalysis is that the ratio of the intensities in the unknown sample to standard intensities, should yield the concentrations of various elements [24].The analysis was done using software called ZAF where Z stands for the atomic number of the element, A and F are the absorbance and fluorescence values. The standard samples for comparison were silicon and germanium.

4.3 X-Ray Diffraction

A given substance always produces a characteristic diffraction pattern, whether that substance is present in the pure state or as one constituent of a mixture of substances.

Principle:
An electron in an alternating electromagnetic field will oscillate with the same frequency as the field. When an X-ray beam hits an atom, the electrons around the atom start to oscillate with the same frequency as the incoming beam. A single atom scatters an incident beam of X-rays in all directions in space but a large number of atoms arranged in a perfectly periodic lattice scatters (diffracts) X-rays in relatively few directions. The periodic arrangement of atoms causes destructive interference of the scattered rays in all directions except those predicted by Bragg law where constructive interference occurs. The waves will be in phase and there will be well defined X-ray beams leaving the sample at various directions. Hence, a diffracted beam is a beam composed of a large number of scattered rays mutually reinforcing one another.

The orientation and interplanar spacing of these planes are defined by the three integers h, k, l called indices. A given set of planes with indices h, k, l cut the a-axis of the unit cell in h sections, the b axis in k sections and the c axis in l sections. A zero indicates that the planes are parallel to the corresponding axis.

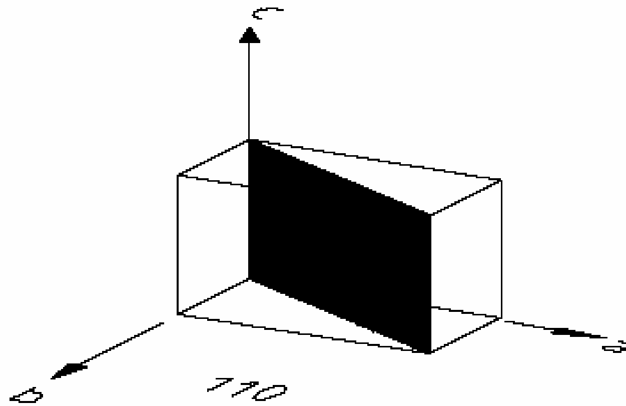

Figure 4.3 shows the (110) plane in a unit cell.

Consider an X-Ray beam incident on a pair of parallel planes P1 and P2 separated by an interplanar spacing d.

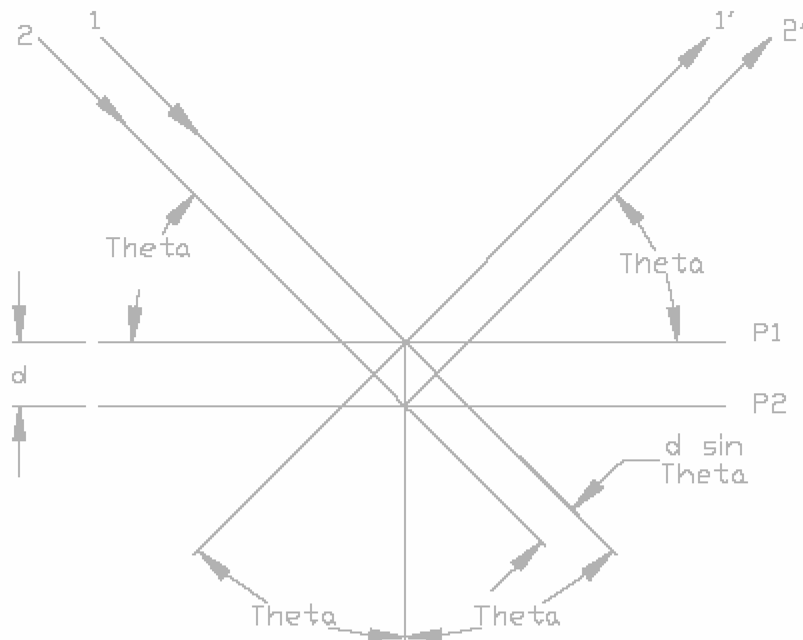

Figure 4.4 shows the XRD setup and principle. (Scintag Inc.)

The two parallel incident rays 1 and 2 make an angle theta (?) with the crystal planes. A reflected beam of maximum intensity will result if the waves represented by 1' and 2' are in phase. The difference in path length between 1 to 1' and 2 to 2' must then be an

integral number of wavelengths, n? [25]. We can express this relationship mathematically in Bragg's law.

2d sin? = n. ?

Phillips X'PERT MRD diffractometer used in these experiments employs copper K-alpha X-ray source of wavelength 1.54187 Å.

4.4 Stress Measurements : Profilometry

Film deposition processes employed in the manufacture of semiconductors and MEMS often have residual stress in both the substrate and the deposited film. Excessive film stresses can lead to deformation, cracking, delamination, shorts and other failures that can render a device unusable.

Principle:

One technique to measure stress is to measure the substrate curvature prior to deposition and re-measure the curvature along the same trace after a film is deposited [11]. The Stress Measurement analysis uses the bending plate method to calculate stress in a deposited thin film layer. This method is based upon changes in curvature and the material properties of the film and substrate.

The key parameters needed to make the stress calculation are the substrate's radius of curvature before and after deposition. If the height of the substrate is expressed as a continuous function of distance along the substrate, $y = f(x)$, then the radius of curvature at any point may be calculated as:

$$\mathbf{R(x) = (1+y'^2)^{3/2} / y''} \quad [26]$$

where $y' = dy/dx$ and $y'' = d^2y/dx^2$

Assuming an initially flat substrate, the stress in the film can then be calculated as:

$$\mathbf{s = 1/6\ (1/R_{post} - 1/R_{pre})\ (E / 1\text{-}?)\ (t_s^2 / t_f)}$$

w h e r e
s = stress in the film
R_{pre} = substrate radius of curvature, before deposition
R_{post} = substrate radius of curvature, after deposition
E= Young's modulus
? = Poisson's ratio
t_s = substrate thickness
t_f = film thickness.

4.5 Fourier Transform Infrared Spectrocopy (FT-IR)

Infrared spectroscopy obtains spectra by first collecting all light as a function of path length between two interfering light beams of a sample using an interferometer, and then performing a fourier transform on the interferogram to obtain the spectrum.

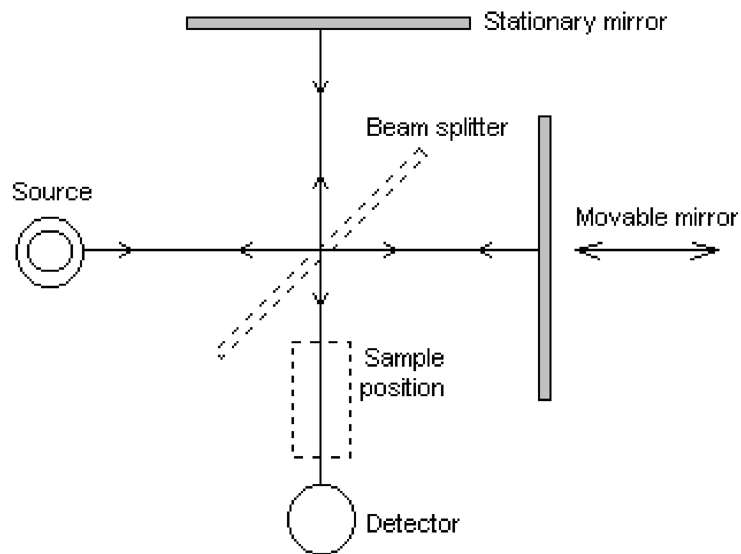

Figure 4.5 shows Michelson interferometer principle.

The interferometer consists of a beam splitter, a fixed mirror, and a mirror that translates back and forth. The beam splitter transmits half of the radiation striking it and reflects the other half. Radiation from the source strikes the beam splitter and separates into two beams. One beam is transmitted through the beam splitter to the fixed mirror and the second is reflected off the beam splitter to the moving mirror. The fixed and moving mirrors reflect the radiation back to the beam splitter. Again, half of this reflected radiation is transmitted and half is reflected at the beam splitter, resulting in one beam passing to the detector and the second back to the source.

FTIR measures the absorption of infrared energy by the molecules in a sample. Many molecules have vibrational modes that absorb specific wavelengths when they are excited. By sweeping the wavelength of the incident energy and detecting which wavelengths are absorbed, a characteristic signature of the molecules present is obtained.

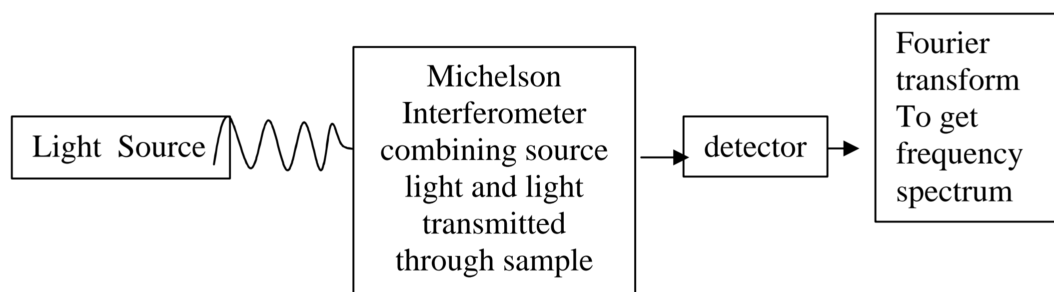

Figure 4.6 Block Diagram showing principle of FTIR
Equipment: Bruker Optik GmbH **Wave number:** 400 cm^{-1} to 4000 cm^{-1}

The FTIR spectrum relies on the interference of light passing through the sample as a function of varying the optical path length of one of the beams. Spectra are normalized by comparison with the interference in the absence of the sample. The frequencies that are transmitted may yield interference fringes, while those that are absorbed yield none. The

spatially modulated interference pattern is fourier decomposed to give the component frequencies which represent the transmission spectrum of the sample. The optical density and absorption are then calculated from the transmission spectrum by $\ln T = C - \alpha d$. T is the transmission, C is some constant over related to transmission in non-absorbing regions and ad is the optical density. The parameter a is the absorption coefficient and d is the sample thickness.

Some features in the spectrum may be due to absorption from contamination on the surface of the sample or to absorption in ambient atmosphere. In addition, the windows, mirrors, and beam splitters in the interferometer can cause some difficulties such as roll-off in the transmission if they become opaque.

4.6 Four Point Probe Measurements:

The purpose of the 4-point probe is to measure the resistivity of a material for either bulk or thin film specimens.

The system consists of four equally spaced tungsten metal tips with finite radius. Each tip is supported by springs to maintain constant pressure and minimize sample damage during measurements. A high impedance current source is used to supply current through the outer two probes; a voltmeter measures the voltage across the inner two probes to determine the sample resistivity.

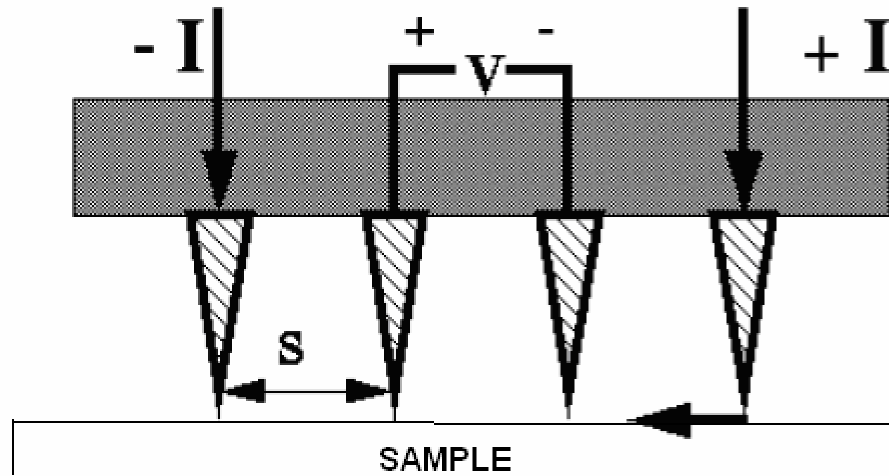

Figure 4.7 shows the principle and setup for a four point probe measurement.[27]

For the resistivity measurements of a thin film,one must consider the following

Area of the film under the inner probe tips = 2.p.x.t

- where x is the distance between the probe tips.

$$R = \int_{x_1}^{x_2} \rho \frac{dx}{2\pi x t} = \int_{s}^{2s} \frac{\rho}{2\pi t} \frac{dx}{x} = \frac{\rho}{2\pi t} ln(x) \Big|_{s}^{2s} = \frac{\rho}{2\pi t} ln2$$

s = distance between the first and second probes

2s = distance between first and third probes.

For R = V/2I , the sheet resistivity for a thin sheet is

$$\rho = \frac{\pi t}{ln2}\left(\frac{V}{I}\right)$$

Sheet Resistivity R_s = ?/ t

R_s = k(V/I) where k is the geometric factor (p/ln 2) *

* Only for large samples compared to probe spacing.

$$R_s = 4.53 * (V/I) *0.0001 *\text{thickness of film in } \mu\text{m.}$$ [28]

4.7 Photothermal Deflection Spectroscopy (PDS)

Photothermal deflection spectroscopy (PDS) is a sensitive method to measure optical absorption and thermal characteristics of a sample. The basis of PDS is a photo-induced change in the temperature state of the sample. Light energy that is absorbed and re-emitted in sample heating. This heating results in a temperature change as well as changes in thermodynamic parameters of the sample which are related to temperature. Measurement of the temperature or density changes that occur due to optical absorption are ultimately the basis for the photothermal spectroscopic methods. In most cases, temperature is the only important parameter [29].

Photothermal deflection spectroscopy is a more direct measure of optical absorption than optical transmission based spectroscopy. Sample heating is a direct consequence of optical absorption and PDS signals are directly dependent on light absorption. Scattering and reflection losses do not produce photo-thermal signals. Therefore PDS more accurately measures optical absorption in scattering solutions, in solids, and at interfaces.

Setup :

Main components used for PDS:

1) sample

2) light used for sample excitation (monochromated white light)

3) light used to monitor refractive index perturbations (laser)

4) an optical detector used to detect the optically filtered probe light (Model SC-4D – UDT sensors Inc.)

5) electronic signal processing equipment

The excitation light, which is normal to the sample surface heats the sample. The probe light, which is parallel to the sample surface in a medium (CCl_4) whose index of refraction is highly temperature sensitive, monitors changes in the temperature of the sample resulting from heating. The spatial and propagation characteristics of the probe light will be altered by the complex refractive index of the sample due to heating. The altered probe light is detected by a position detector which measures the absorption due to change in the temperature of the medium.

Spatial gradients in refractive index result in a direction change in the propagation of the probe of light. Thus light will exit a medium with a refractive index gradient at an angle relative to the incident ray. This bending of the light ray can be qualitatively related to the absorption in the sample

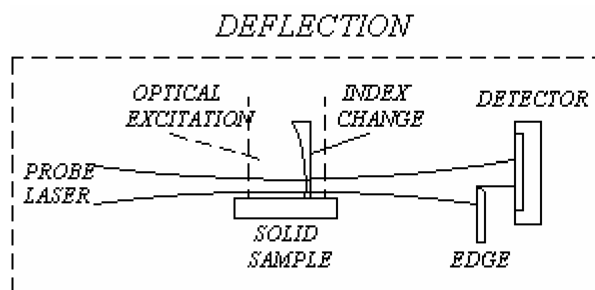

Figure 4.8 shows the principle behind Photohermal deflection spectroscopy. [30]

4.8 Atomic Force Microscopy (AFM)

Atom force microscopy is a scanning probe technique where a sharp tip on a cantilever scans the surface. Forces (Van Der Walls, Coulomb and Meniscus) acting between the cantilever and the surface, results in deflection of the lever from its equilibrium position. Measuring deflection as a function of time lets us form an image of the surface close to atomic resolution.

Van der walls forces between two atoms results from fluctuations in the charge density of the atomic cores and the surrounding electrons. Coulomb force is due to interaction between charged particles or objects and meniscus force arises from surface tension in a water-meniscus that spans between tip and surface. The Meniscus is present when scanning in gas-phase or in vacuum with sufficiently small tip-surface distances.

The equipment used was a Pacific Nanotechnology Nano-R™ AFM and surface morphology was characterized in the “close-contact” mode. The close-contact mode where the tip scans the sample in close contact with the surface is the common mode used in the force microscope. The force on the tip is repulsive with a mean value of 10^{-9} N.

This force is set by pushing the cantilever against the sample surface with a piezoelectric positioning element. The deflection of the cantilever is sensed and compared in a DC feedback amplifier to some desired value of deflection. If the measured deflection is different from the desired value, the feedback amplifier applies a voltage to the piezoelectric element to raise or lower the sample relative to the cantilever to restore the desired value of deflection. The voltage that the feedback amplifier applies is a measure of the height of features on the sample surface [42].

5.0 RESULTS:

5.1 Growth Conditions:

Silicon Germanium (SiGe) films were grown in a Plasma enhanced chemical vapor deposition (PECVD) system using silane (SiH_4) and germane (GeH_4) as precursor gases, and diborane (B_2H_6) and phosphine (PH_3) as dopants. Hydrides are used as precursor gases because hydrogen scavenges oxygen which reduces oxide inclusions in the film

The SiGe films were grown on Corning 7059 glass and n-type diced 4" Silicon substrates. The growth conditions to achieve a Si_xGe_{1-x} concentration where x=0.8 for boron and phosphorous doped samples are listed below.

Boron doped samples.

Silane (SiH_4) = 42 sccm; Germane (GeH_4) = 4 sccm ; 1% Diborane in H_2 (B_2H_6) =14 sccm; Temperature > 550°C; Pressure = 500 mTorr.

Phosphorous doped samples:

Silane(SiH_4) = 43.6 sccm; Germane(GeH_4) = 2.8 sccm ; Phosphine (PH_3) =0.80 sccm; Temperature > 550°C; Pressure = 440 mTorr.

5.2 Energy Dispersive X-Ray analysis (EDX):

To quantify the concentration of germanium (Ge) and silicon (Si) in the sample, EDX analysis was done. Data from samples grown thicker than a micron to prevent sampling of the substrate are shown below. The data was used to quantify the composition in the film as well as compare it with compositions obtained by x-ray diffraction (XRD)

In figure 5.1, the Ge peaks are at 1.08 keV and 1.13 keV. The silicon peak is at 1.74 keV. We see no presence of contaminants. Oxygen is also below the noise level in the spectrum indicating that the oxygen contaminant is less than 1 at. %. The peak at 0 keV is known as the zero strobe peak and is an artificial peak centered on zero energy from which offset can be monitored. The results were verified by X-ray diffraction using Dusmukes law [13]. The concentration of the SiGe alloy across the sample was uniform with a deviation of +/- 2 at. %. Annealing the samples did not result in any change to the atomic composition of Si and Ge in the samples or any significant increase in oxygen contamination. The compositional results obtained by EDX and XRD agreed.

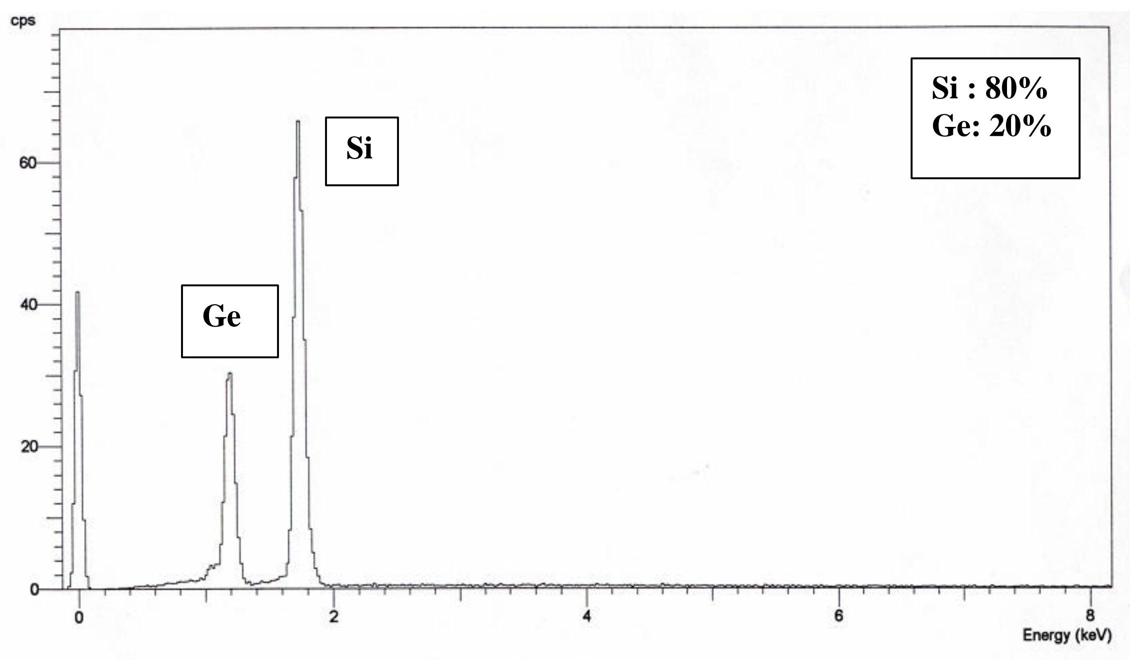

Figure 5.1 shows the intensity of the Si and Ge peaks in a SiGe sample.

5.3 X-Ray Diffraction:

As grown samples:

X-Ray diffraction was performed on samples on 7059 glass substrates. The X-ray results were used to determine the crystallite texture of the samples. Only data for sample ID 050531 are shown. See appendix for other samples.

.

For a Ge concentration of 20% in the SiGe alloy, we find predominantly (111) and (110) texture. The lattice spacing was calculated from Dismukes law [16] which gives the lattice constant of the SiGe alloy as a function of germanium concentration as follows

Lattice constant $a(x) = (5.431 + 0.20x + 0.027x^2)$ **Å** * [16] (1)

* where x is atomic fraction of Ge in alloy

Sample :050531

2Theta (2?)	d spacing (Å)	$h^2+k^2+l^2$	Orientation
27.35	3.25	2.83	111
45.5	1.99	7.6	220
53.9	1.7	10.45	311
72.8	1.3	17.7	331

Table 5.1 shows XRD data for as grown 20% SiGe phosphorous doped sample.

Annealed samples:

The samples were annealed at temperature varying from 525 ^{o}C to 650 ^{o}C in an atmosphere of Nitrogen. The annealing times were also varied from 30 min to 15 hours. Table 5.2 shows X-ray diffraction data for sample annealed for 30 minutes at 575 ^{o}C.

Sample: 050531.

2Theta (2?)	**d spacing (Å)**	**h^2+k^2+l^2**	**Orientation**
27.4	3.25	2.83	111
28.2	3.16	3.0	111
45.5	1.99	7.55	220
46.9	1.94	7.95	220
53.75	1.70	10.4	311
55.6	1.65	11	311
73.0	1.3	17.7	331
75.4	1.26	18.84	331

Table 5.2 shows data for annealed sample doped with phosphorous

On annealing, we see an additional peak closer to the (110) and (111) planes as observed in the as-grown crystal. We see two peaks, one from the as grown crystal and a peak due to annealing of the samples. The peak that appears on annealing has the alloy concentration of 20% Ge as identified by EDX analysis.

X-Ray Diffraction

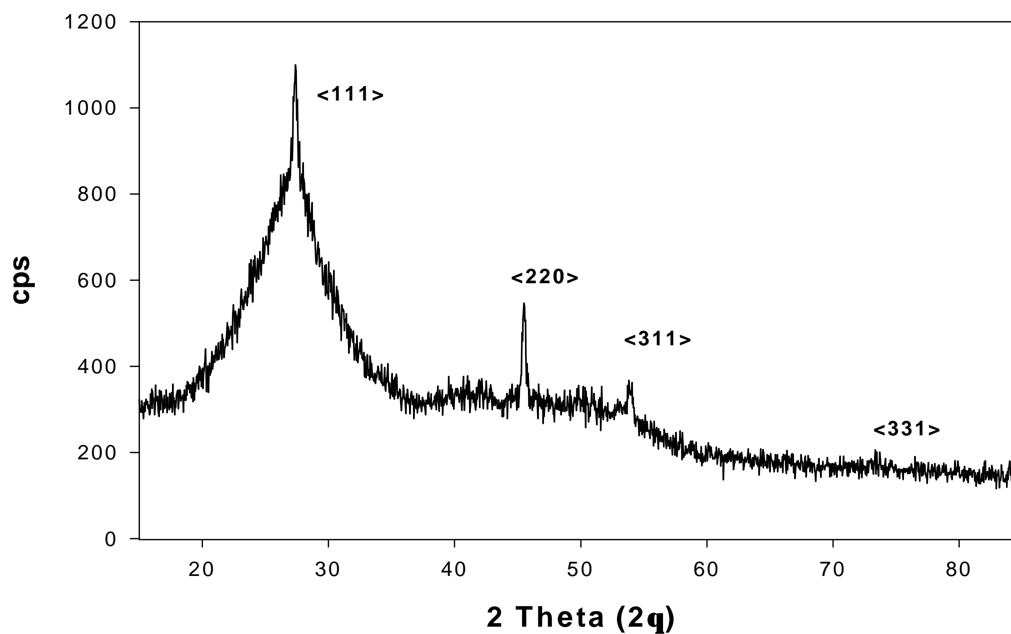

Figure 5.2 shows XRD peaks for as grown sample 050531

X-Ray Diifraction

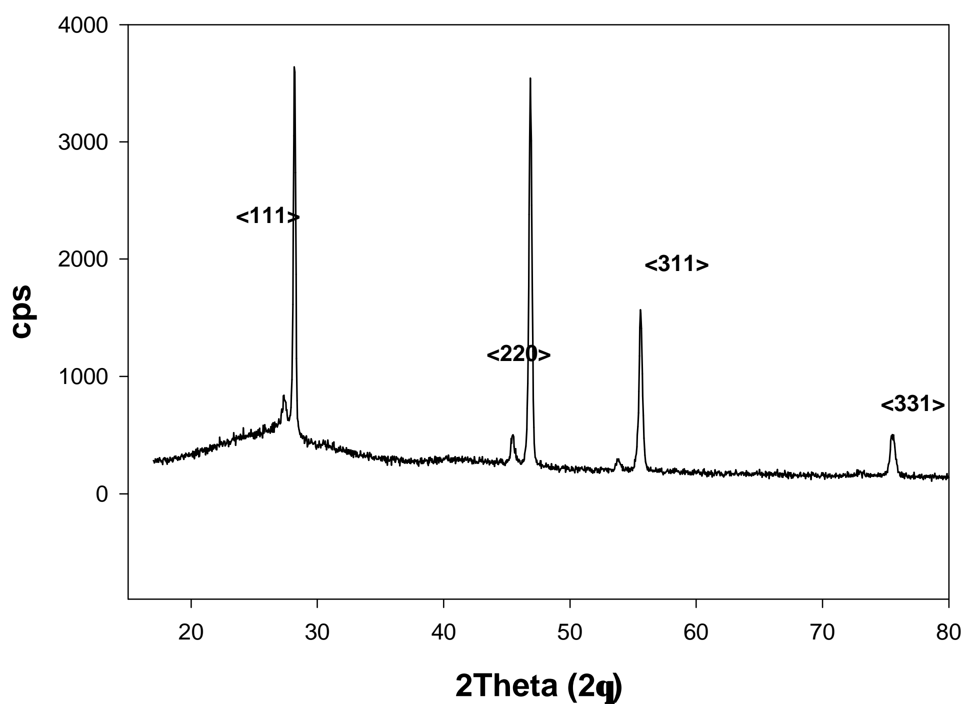

Figure 5.3 shows diffraction peaks for annealed sample 050531.

5.4 Stress Measurements:

Excessive film stresses can lead to deformation, cracking, delamination, shorts and other failures in a device. Accurate assessment of the deformation caused by film stress is therefore critical for developing quality films. Average stress was measured by the bending plate deflection method described earlier.

As grown films:

Stress (MPa)	Pressure (mTorr)	Temperature (ºC)	Power (watts)	Thickness (µm)	Germanium Conc.%
-20.4	440	595	20	1.8	20
-75.4	430	595	19.5	3.75	25
-161	440	587	19	2.5	30
-227	460	605	16	3.75	45
18	440	590	20	2.5	20
-10	440	592	20	1.8	20
-44.7	440	595	20	0.7	20

Table 5.3 details the effect of deposition parameters on the stress in SiGe alloys of different compositions.

Annealed Samples:

Anneal temp (ºC)	Anneal time (hours)	Stress (GPa)	Ge Conc%	Power (Watts)	Thickness µm	Sample ID
685	0.17	1.56	20	18	2.4	050316
525	3	0.178	22	18	3.75	050311
525	15	0.868	22	18	1.8	050309
550	17	1.05	25	19	2.5	050422
650	0.5	1.53	20	20	2.5	050530
525	15	1.037	20	20	1.9	050531
525	0.5	.160	20	20	1.9	050531
550	0.5	.165	20	20	0.8	050601
575	0.5	1.2	20	20	0.8	050601

Table 5.4 shows stress data for annealed samples with different germanium concentrations.

Stress Measurements

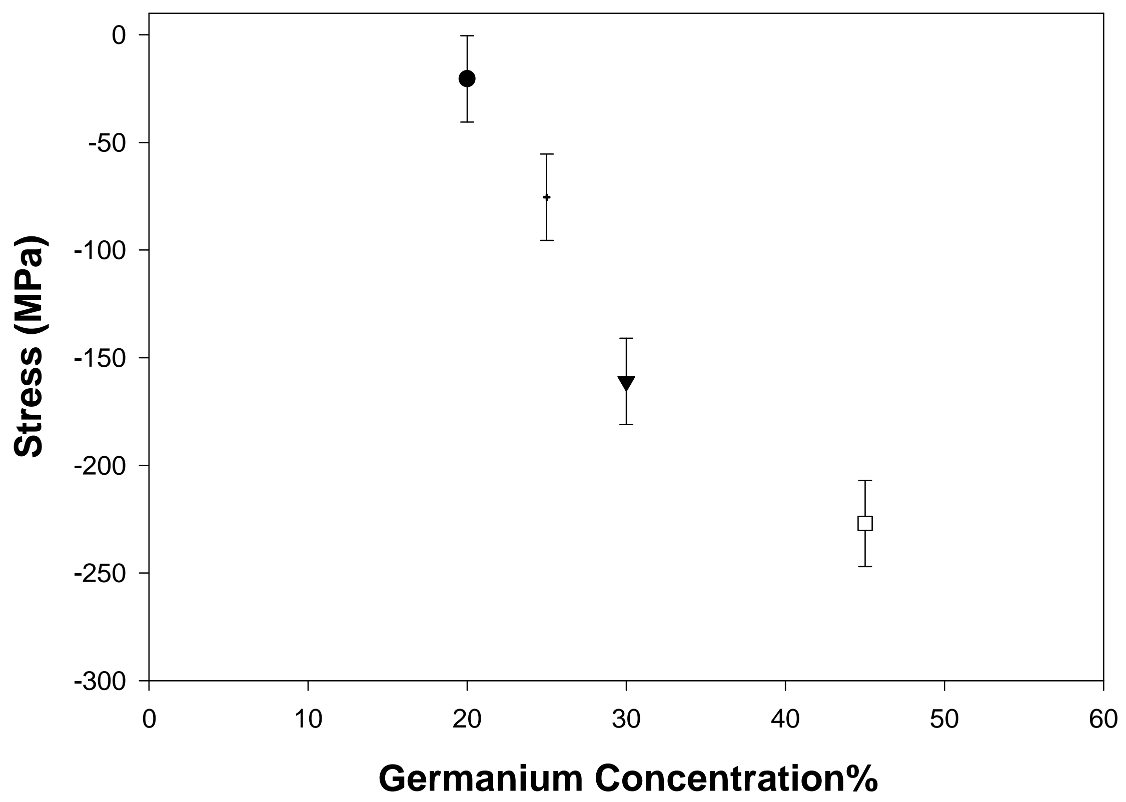

Figure 5.4 showing variation of stress with Ge. conc %.

? Pressure:440 mtorr;temperature:594 ºC; power:20watts;thickness:2.5µm
· Pressure: 430 mtorr;temperature:590 ºC; power :19.5 watts; thickness:3.75 µm
? Pressure :460 mtorr; temperature : 587ºC; power:19 watts; thickness : 2.6 µm
? Pressure : 460 mtorr, temperature:605 º C; power : 16 watts,thickness:3.75µm.

Figure 5.4 shows varaiation of stress with Ge concentration%

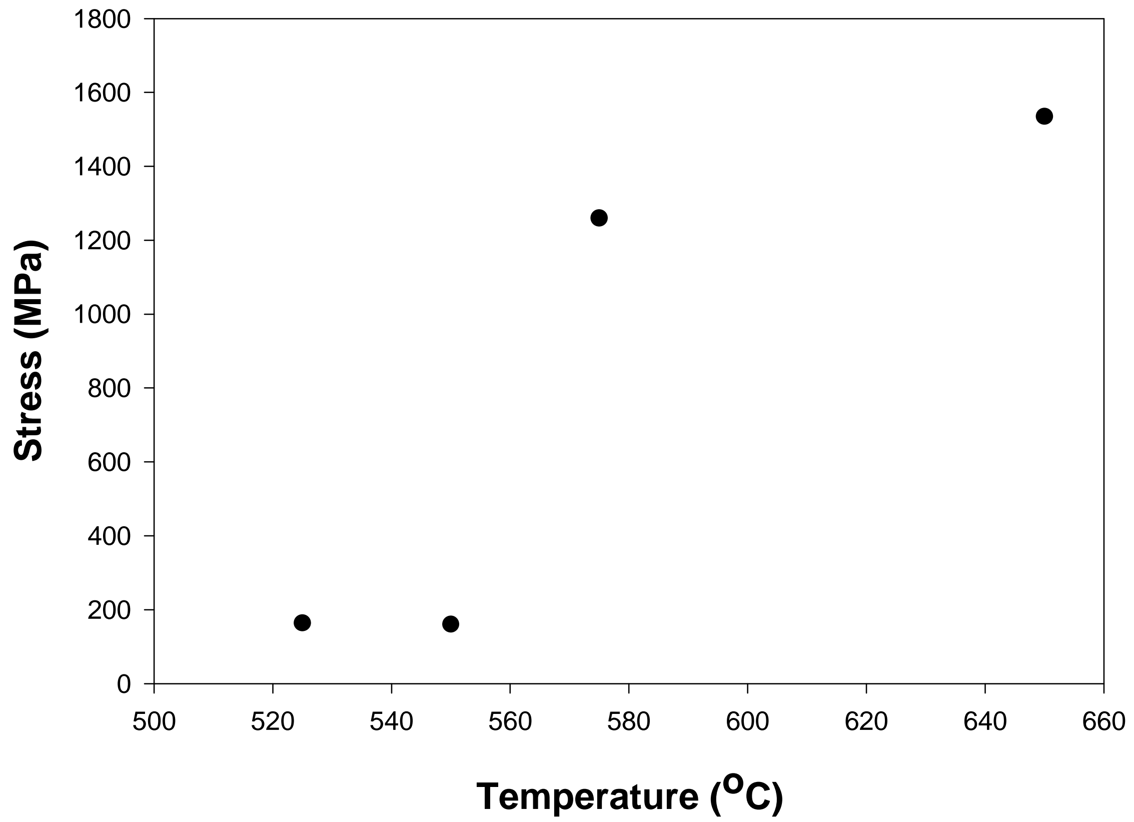

Figure 5.5 shows the effect of annealing temperature on stress for Ge:20%
(Error bars are size of the data points.)

? Anneal time was 30 minutes for 20% Ge concentration.

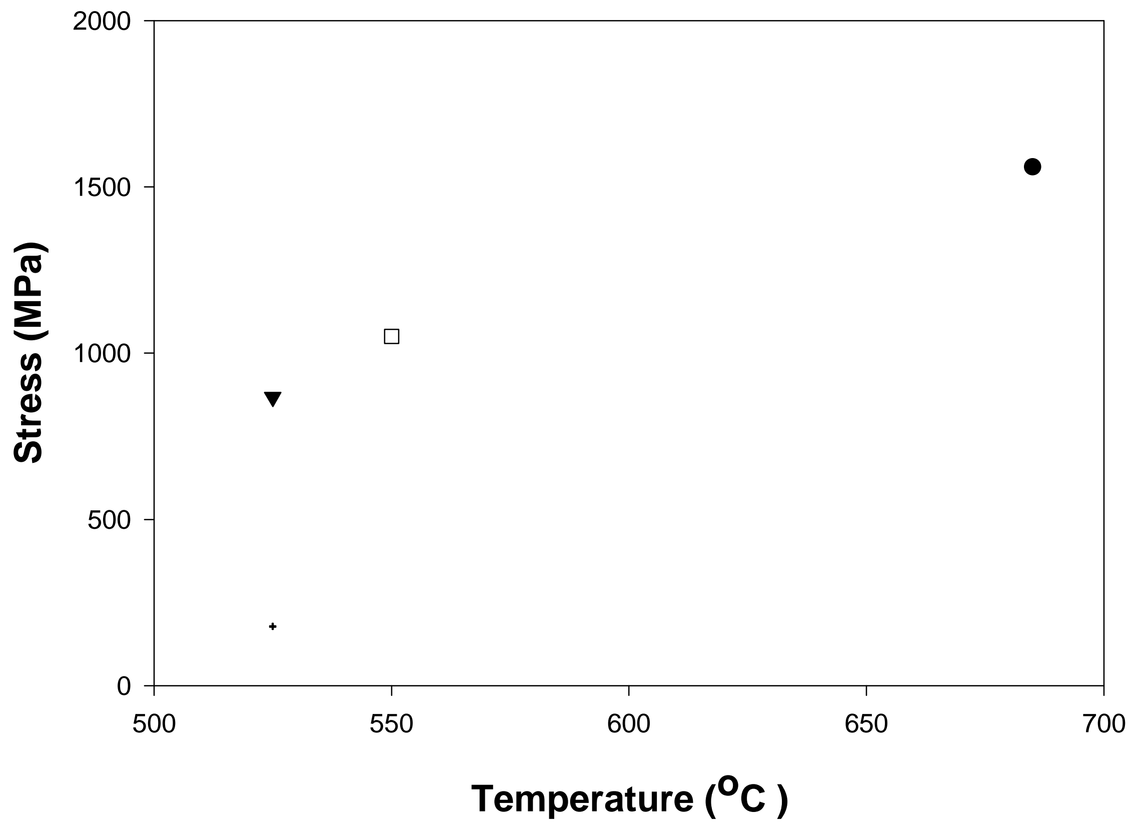

Figure 5.6 shows the stress variation with annealing temperature
(Error bars are size of the data points.)

? Ge:22% concentration; 3 hours anneal time
? Ge:22% concentration; 15 hours anneal time.
? Ge 25% concentration; 17 hours anneal time.
? Ge:20% concentration ; 0.17 hours anneal time

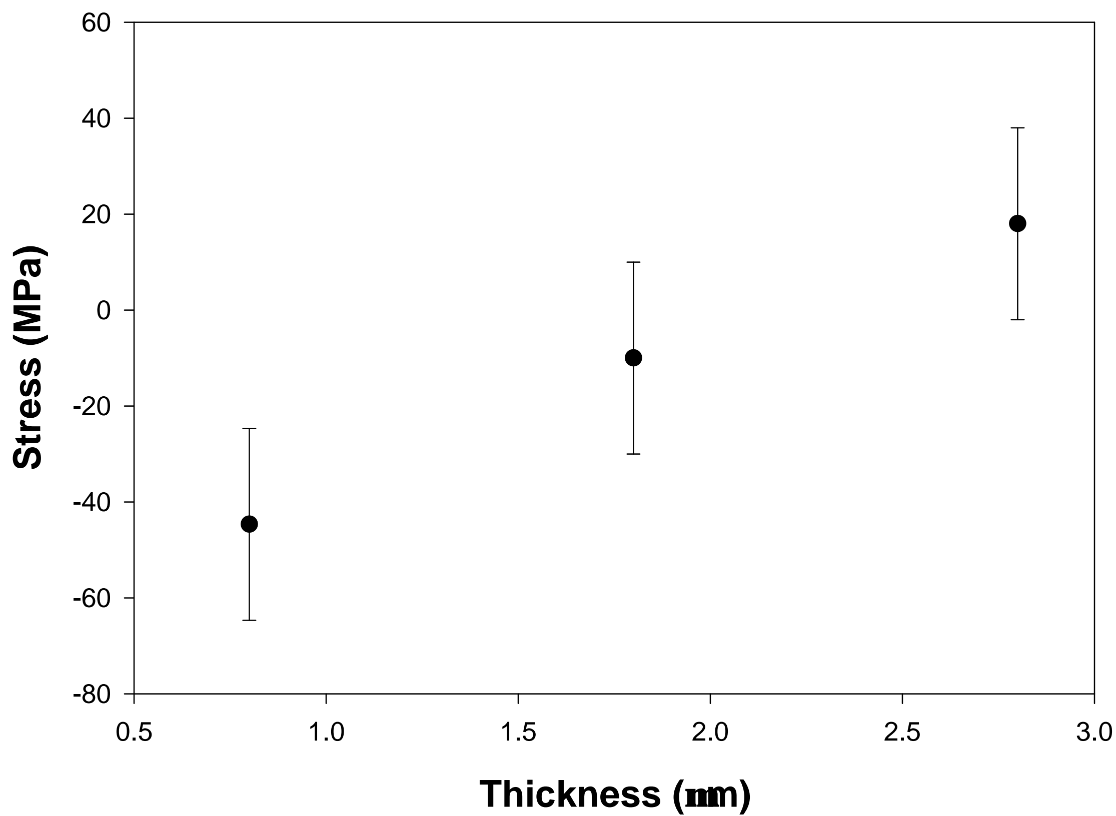

Figure 5.7 shows the variation of the stress with thickness for 20% germanium concentration

? Germanium concentration: 20%.

5.5 Fourier Transform Infrared Spectroscopy (FTIR):

Infrared spectroscopy data was collected from SiGe samples deposited on silicon wafers, which were polished on both sides. Figure 5.8 shows the absorption spectrum of the SiGe films for a boron-doped sample. The boron doped sample has a Ge concentration of 20% while the phosphorous doped sample has a Ge concentration of 30%.

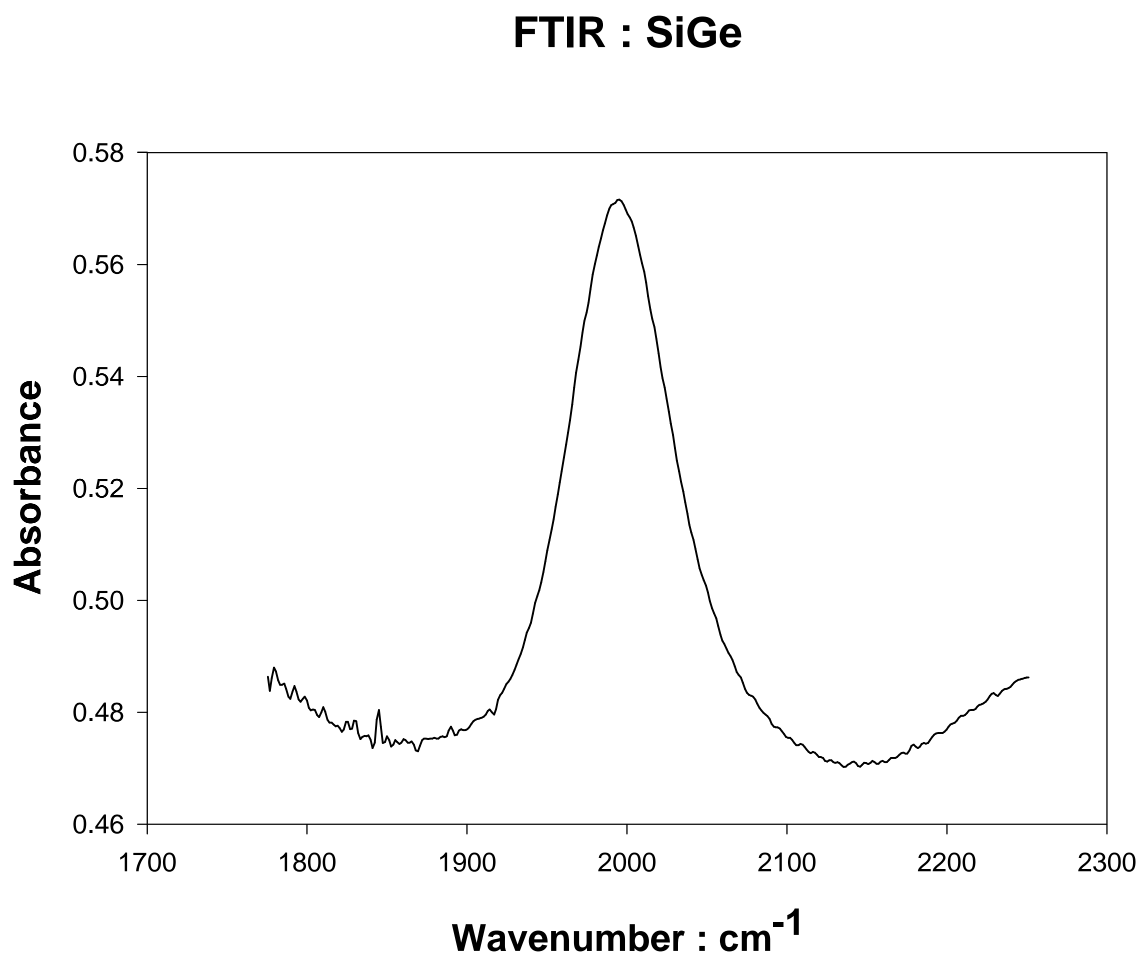

Figure 5.8 shows convoluted Si-H and Ge-H peaks from 1950 to 2050 cm^{-1} for a boron doped sample. The peaks correspond to Si-H and Ge-H stretch modes.

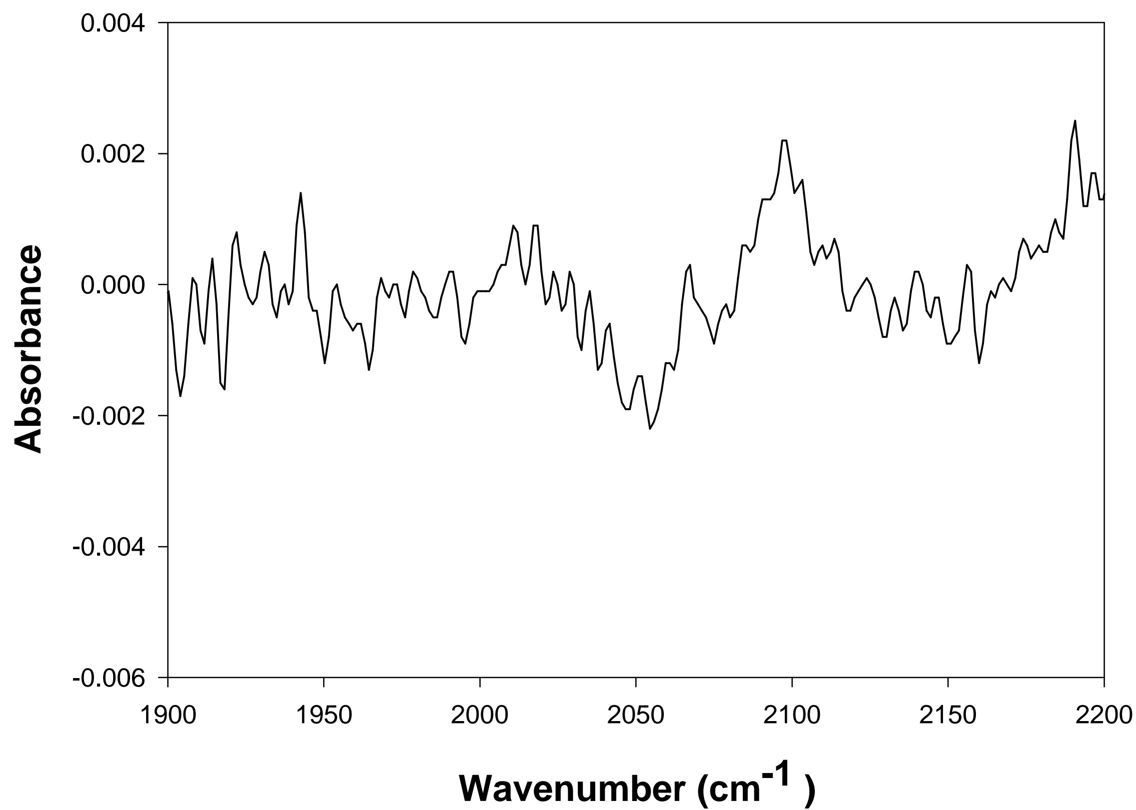

Figure 5.9 shows the absence of Si-H and Ge-H peaks after annealing in boron doped sample.

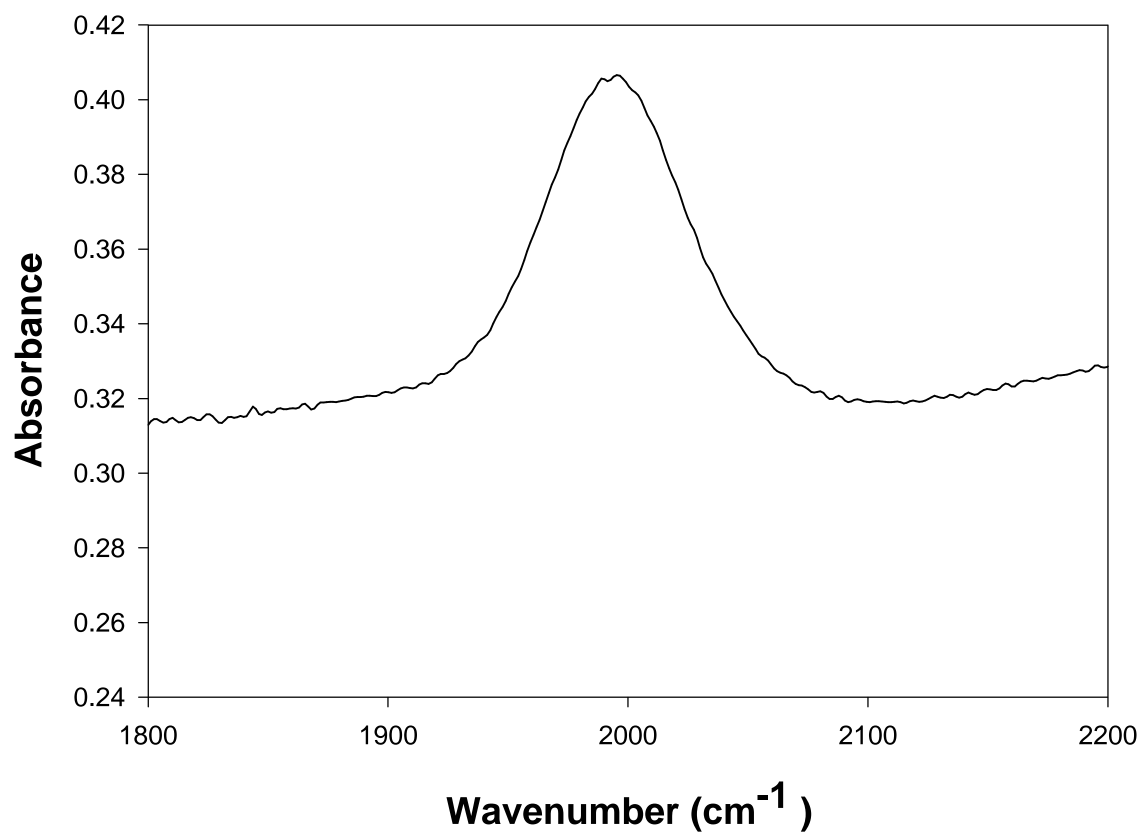

Figure 5.10 shows convoluted Si-H and Ge-H peaks at about 2000 cm^{-1} and 1950 cm^{-1} for phosphorous doped sample.

5.6 Surface texture

Surface texture of the samples was measured using Atomic Force Microscopy (AFM). Measurements were made on a boron-doped sample as well as phosphorous-doped samples at Weber State University.

Boron doped samples:

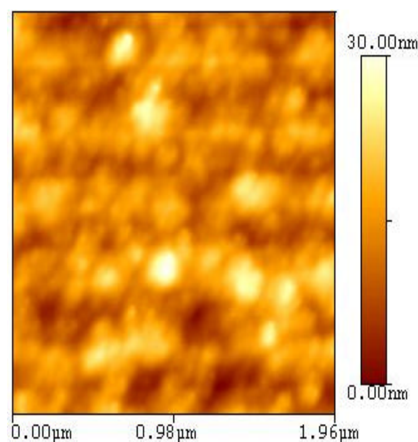

Fig 5.11 Annealed boron doped sample
Surface texture ranges from 20 nm to 150 nm
No structure resolved in large clusters

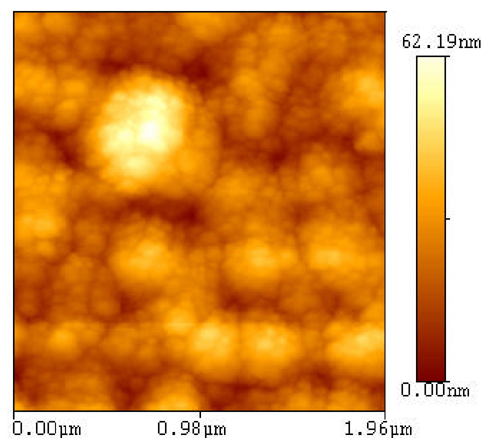

Fig 5.12 As-grown boron doped sample.
Surface texture ranges from ~20 nm to ~500 nm
Large clusters are aggregates of smaller clusters.

Phosphorous doped samples:

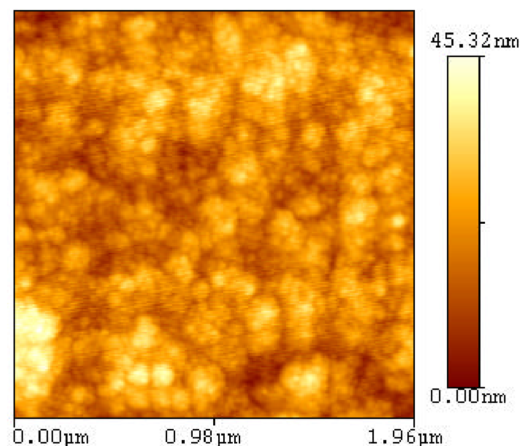

Fig 5.13 Annealed phosphorous doped sample
Surface texture ranges from 20nm to 200nm
Large ckusters are aggregates of smaller clusters

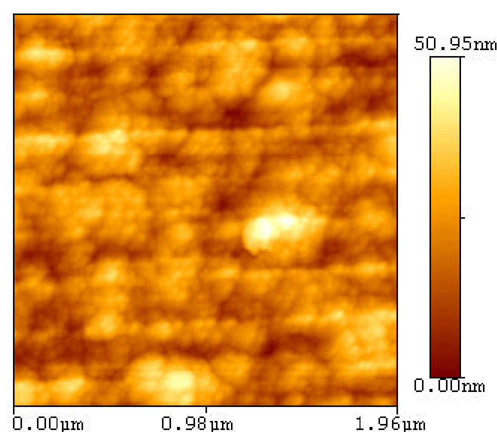

Fig 5.14 As-grown phosphorous doped sample
Surface texture ranges from 20nm to 400 nm
Some structure resolved in larger clusters

5.7 Resistivity measurements:

To grow crystalline material, deposition runs were performed at temperatures greater than 550 ℃ for boron-doped and phosphorous-doped samples for low germanium concentrations. Resistivity was measured using the four point probe. The SiGe layers were grown on a silicon substrate, which had a 500nm thick thermal oxide grown on it

Boron doped SiGe samples:

Germanium concentration.%	**Deposition temperature (ºC)**	**Resistivity (mO-cm)**
100	504	1.3
75	560	3.4
20	585	44

Table 5.5 shows resistivity for different germanium concentrations.

Phosphorous doped SiGe samples:

Germanium concentration%	**Deposition temperature (ºC)**	**Resistivity (O-cm)**
30	590	6.2
25	595	8.3
20	585	6.8

Table 5.6 shows resistivity for different germanium concentrations

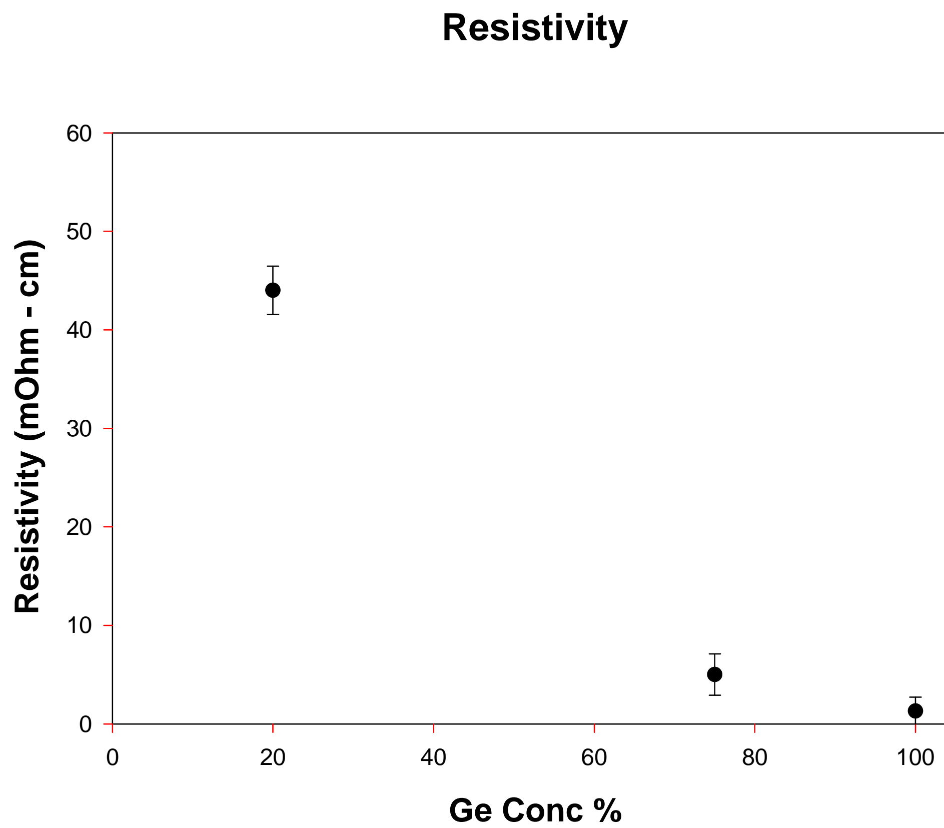

Figure 5.15 shows resistivity for as-grown boron-doped samples.

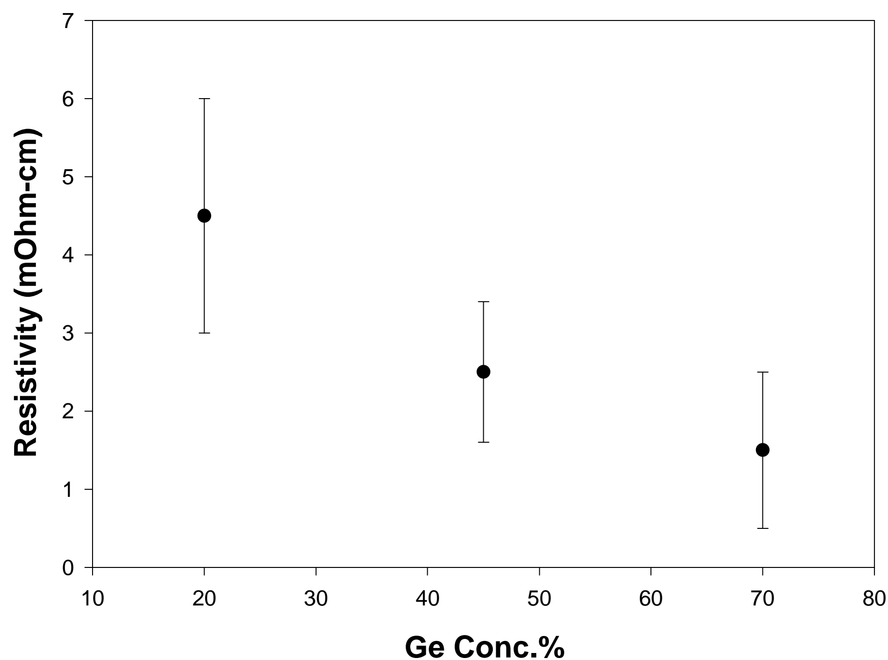

Figure 5.16 shows resistivity data for annealed, boron-doped samples.

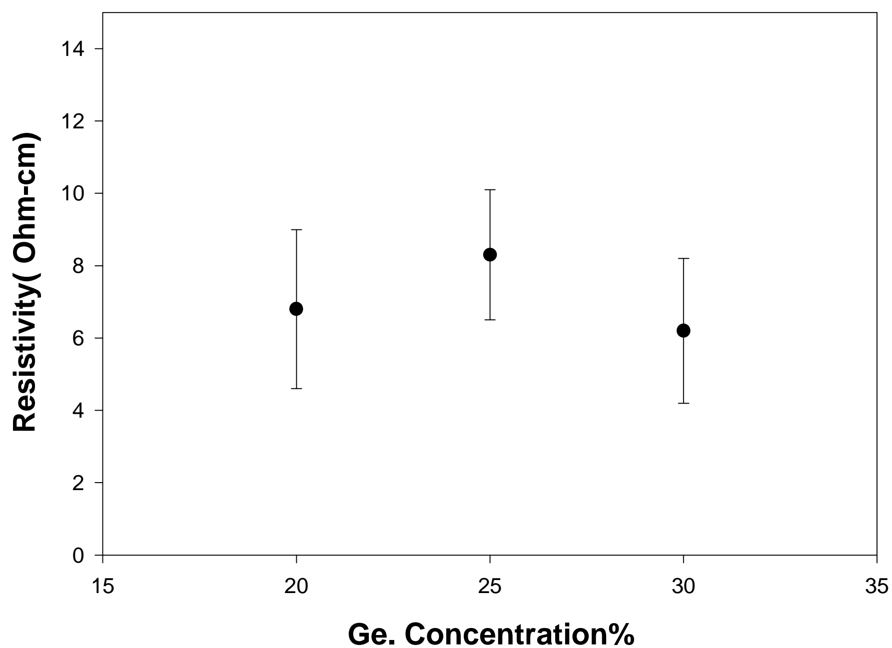

Figure 5.17 shows resistivity for phosphorous doped samples

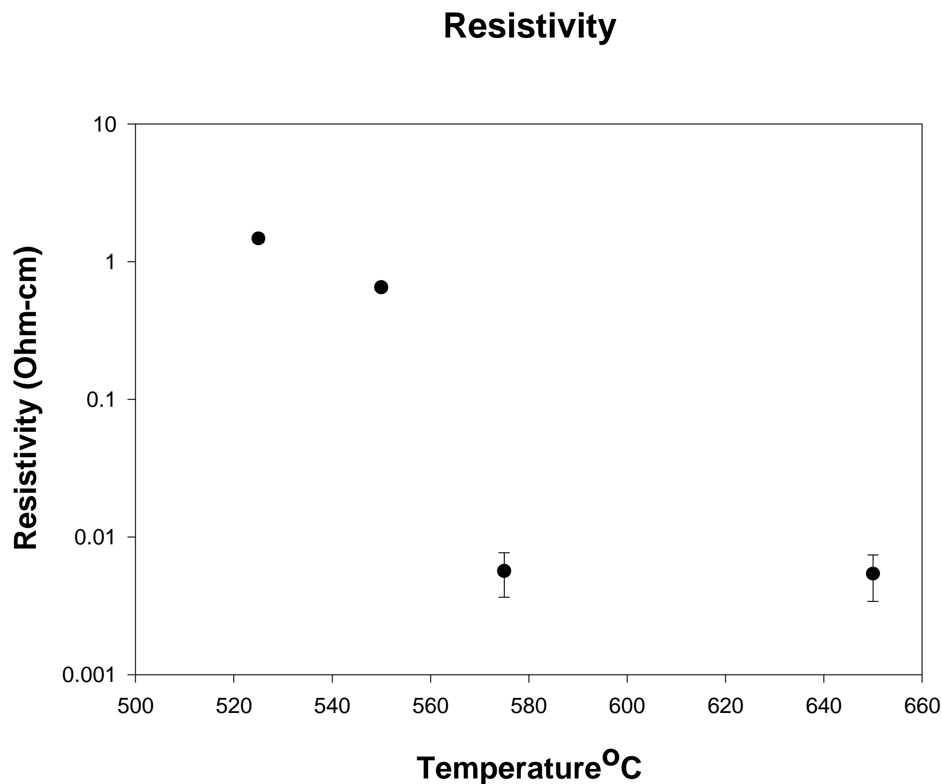

Figure 5.18 shows resistivity for phosphorous doped films, as a function of annealing temperature for 20% germanium concentration. The annealing time was 30 minutes at each temperature.

5.8 Photothermal Deflection Spectroscopy (PDS):

Photothermal deflection spectroscopy (PDS) gives valuable quantitative and qualitative information about the Density of States in SiGe alloys. A sharp Urbach tail indicates a low density of shallow gap states [29]. A low absorption coefficient in the subbband absorption region implies a low density of deep defect states. PDS is also used to determine the optical bandgap of the sample. The germanium content defines the optical energy gaps according to the relation

$\mathbf{E_g = (1.85 - 0.85x)}$ [32] where x is the atomic fraction of germanium in amorphous material.

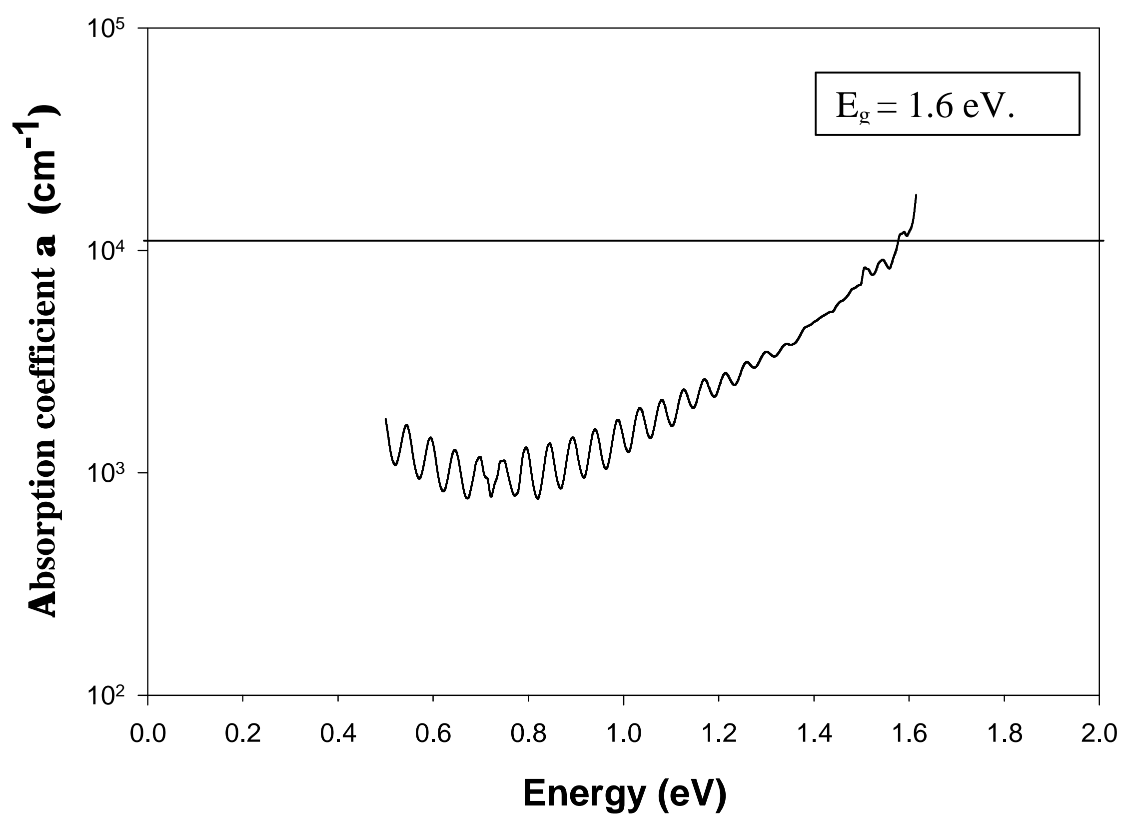

Figure 5.19 shows sub-band gap absorption and band gap of annealed Si_xGe_{1-x} with x=0.78.

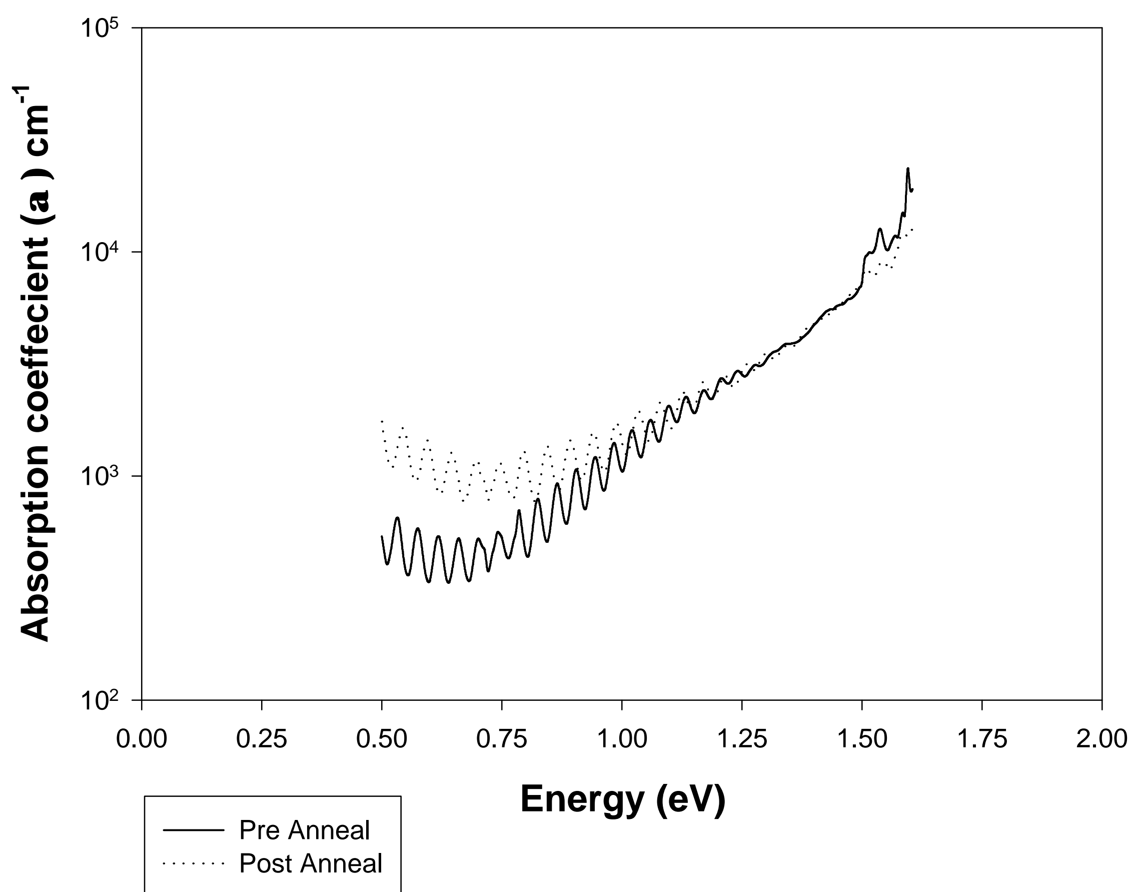

Figure 5.20 shows enhanced absorption in the sample after annealing, which is probably due to free carrier absorption.

6.0 DISCUSSION:

6.1 Growth conditions and EDX:

Silicon germanium (SiGe) thin films doped with either boron or phosphorous were grown using the Plasma Enhanced Chemical vapor Deposition (PECVD) system. Hydrides are used as precursor gases because hydrogen scavenges oxygen and reduces the oxygen contaminant inclusions in the film. The dissociative reactions occurring within the chamber are

Silicon Germanium (SiGe) films deposited with high Ge concentrations resulted in the large surface roughness. Growth rates were low for high Ge concentrations in agreement with previous results of Bang *et al* [16]. In addition growth temperatures were lower resulting in thinner films. For high Ge concentrations and lower growth temperature, the growth rate was slower. Growth rates increased from 0.18 nm/sec for 65% Ge to 0.8 nm/sec for 20% Ge. The growth temperatures also increased for 20% Ge in order to grow the material poly-crystalline.

For low germanium concentrations and increased silane flow rates, growth rate increased by a factor of 7 at deposition temperatures greater than 560 ºC. Resistivity is high for

lower Ge concentrations in as-grown doped samples shown in table 5.6 and 5.7. Higher resistivity for as-grown samples suggests appreciable amorphous content present in the films.

Germanium incorporates readily than Si for similar silane and germane flow rates. Increasing the silane flow rate increases the partial pressure of silane thereby decreasing the probability that a Ge atom will deposit on the surface of the film [21]. EDX analysis reveals silicon and germanium peaks with minimal presence of oxygen in the film. Compositional analysis across the length of the film yielded uniform compositions of Si and Ge within an error of +/- 2 at. %.

6.2 X-Ray Diffraction (XRD):

X-Ray diffraction yielded predominantly (111) and (110) orientation in as- grown films. Lattice constant is calculated from Dismukes law given by (1) in results section.

The {h k l} crystallographic planes is calculated using the equation given below

$$\textbf{(Lattice constant ? / Interplanar spacing (d))}^2 = \mathbf{h^2 + k^2 + l^2}$$

{h k l} = principal crystallographic planes in a unit cell.

As grown samples:

For ss grown samples at 20% Ge concentration, we see have predominantly (111) and (110) crystal planes as shown in table 5.1. The <hkl> values are shifted because the crystals grow with higher Ge concentrations. As shown in the table below, the values correspond to a germanium concentration of approximately 90%.

The growth of samples with 20% Ge content was initially deposited with pure germanium in order to seed crystallinity. This procedure favors crystallites that grow in the same direction with enhanced Ge concentrations.

The (111) plane is the most preferred growth direction in as grown samples as it is the most dense orientation. The table below shows the <hkl> values adjusted for a Ge concentration of 90%.

Sample: 050531.

2Theta (2?)	d spacing (Å)	$h^2+k^2+l^2$	Orientation
27.35	3.25	3.01	111
45.5	1.99	8.0	220
53.9	1.7	11	311
72.8	1.3	18.83	331

Table 6.1 shows data for as grown sample adjusted for higher Ge concentration (90%)

Annealed samples:

On annealing, we see an additional peak closer to the (110) and (111) planar orientations obtained in as-grown crystallites seen in Figure 5.3 and Table 5.2l. We see two peaks, one from the as grown crystal and a second peak due to annealing of the samples. The peak that appears on annealing has the alloy concentration 20% Ge verified by XRD analysis.

The peaks from as-grown crystallites do not grow in intensity when annealed. The crystallites in the annealed samples grow preferentially in the <110> direction for thicker

films. Films thinner than 2 μm have a preferentially grow in the <111> direction. We also see <100> directions for annealed boron doped samples, which indicate random crystallites of these orientations.

6.3 Stress Measurements:

The average stress was measured in the samples by the bending plate deflection method. The as-grown thin film stress was measured by measuring the surface of the substrate before and after deposition of the film.

As grown film:

The stress tends to increase with increasing germanium concentrations as shown in figure 5.4. This trend is consistent with the fact that the surface roughness increases for higher germanium concentrations [1]. Pressure and temperature also do not have any major effect on the stress.

For lower deposition pressures and lower germanium concentrations, the tensile stress value in as grown films is as low as 18 MPa tensile. Thicker films tend to have less compressive stress in comparison to thin films for a similar germanium concentration as seen from table 5.4 and Fig. 5.7.

Stress: Annealed films.

The stress in annealed films depends on annealing temperature and annealing time. The films were annealed in an atmosphere of N_2 for varying time periods. The films grow under compressive and change to tensile stress when the stress is released on annealing. For lower annealing temperatures (= 550 °C), the film has smaller stress but higher resistivity. As the annealing temperature increases, the stress also increases in for fixed germanium concentration as seen in Fig. 5.5.

The films contain less hydrogen for depositions at higher temperatures because the hydrogen diffuses out of the samples. For annealing time upto 17 hours, the film does not crack after the hydrogen diffuses out. For annealing time greater than 20 hours, the films crack due to a large amount of tensile stress. For a short annealing time and low annealing temperatures, the stress in the sample is low, but we obtain some amorphous component as visible from the PDS spectra.

6.4 Fourier Transform Infrared Spectroscopy (FTIR):

FTIR was performed on SiGe films with 20% and 30% Ge concentration grown on silicon wafers that were polished on both sides. The FTIR spectra reveals hydrogen bonded to silicon as well as germanium. The FTIR spectra in the range 1700 to 2200 cm^{-1} show Ge-H and Si-H stretching modes. The Si-H stretch mode and Ge-H stretch mode are present at 2000 cm^{-1} and 1950 cm^{-1} respectively [22,23]. The hydrogen bonds

selectively to Silicon since the peak is closer to 2000 cm^{-1} (Si-H stretch mode) as shown in figure 5.8 .Higher deposition temperatures have resulted in less hydrogen in the films [33] and hence the absence of Ge-H and Si-H wagging modes in the film. The binding energy of Ge-H is less than Si-H and at high deposition temperatures; the Ge-H bond is comparatively unstable resulting in probably lesser hydrogen bonded to Ge.

Annealing of the film resulted in release of hydrogen from the sample, which reduces the intensities of the Si-H and Ge-H peaks. There is a definite reduction of hydrogen in the sample upon annealing as shown in Fig. 5.9.

6.5 Surface texture:

As-grown samples had surface texture varying from 20nm to about 500nm. The grain size of the amorphous film is likely formed due to deposition of predominantly Si clusters on the film. The larger aggregate grains were a conglomeration of smaller Si clusters. Annealed sample grain sizes vary from 20nm to 200 nm. When films crystallize coalescence of grains normally occurs through various nucleation and grain growth mechanisms [42]. Surface texture was similar for boron and phosphorous doped films.

6.6 Resistivity Measurements:

For increased Ge concentrations, the resistivities of the as-grown samples are lower. Deposition temperatures can be lowered for higher Ge concentrations. As the Ge concentration decreases, the resistivity of the film decreases and deposition temperature has to increase in order to grow the poly-crystalline films. The lower resistivity is

attributed to an increase in the hole mobility and dopant activation as the Ge concentration increases. Annealing boron-doped samples yielded resistivity as low as 1.3 mO-cm. The resistivity varied with Ge concentration from 1.3 mO-cm to 4.6 mO-cm.

Phosphorous-doped samples have higher resistivity than boron-doped samples. This fact is attributed to the increased mobility but decreased effective carrier concentration in phosphorous-doped samples [16]. Annealed phosphorous-doped samples have a resistivity of about 1.4 mO-cm. Annealed boron doped samples do not have as large a change in resistvity as in phosphorous-doped samples after annealing.

6.7 Photothermal Deflection Spectroscopy (PDS):

PDS is used to determine the optical bandgap in the sample. Germanium content defines the optical energy gaps according to the relation

Eg = (1.85 – 0.85x) [32] where x is the fraction of germanium concentration

In figure 5.19, the concentration of germanium in the sample is 22% as determined by Energy Dispersive X-ray analysis (EDX). The 10^4 cm^{-1} line signifies the approximate band edge of the sample and hence the optical band gap of the alloy. The equation gives the energy gap to be 1.66 eV while the PDS plot gives the approximate band gap value to be 1.6 eV.

The slope of the sub band gap absorption tail suggests the sample is not completely crystalline in nature and has amorphous content. The high absorption in the sample is probably due to free carrier absorption. Drude theory predicts materials having high free

carrier densities become dielectrics at high frequencies. The frequency at which this occurs is called the plasmon frequency.

Plasmon frequency ($?_p$) = Ne^2 / me_o

= 4e26 * $1.602e\text{-}19^2$ / 9.11e-31 * 8.854e-12= 1128 THz (0.743 eV)

Where N = Doping density in m^{-3}. e = electron charge = 1.602 E-19 coulombs.

m = effective mass e_o = permittivity in free space = 8.854e-12 F/m.

7.0 FUTURE WORK/SUMMARY:

a) Thin film Si_xGe_{1-x} with Ge concentration of about 20% were successfully developed with low as-grown stress of about 18 MPa tensile and resistivities as low as 1m? -cm. The sample was grown with a lower thermal budget at the rate of 0.8 nm /sec.

b) Growth rates increase by a factor of 7 for lower Ge concentrations and higher growth temperatures.

c) X-Ray diffraction of as-grown samples indicates crystallites with high Ge content in the alloy. Crystallites in the (111) and (110) planes are predominantly found. Annealing the samples lead to formation of dual peaks with different Ge concentrations but similar crystallite directions. The diffracted peaks from annealed samples have concentrations that compare favorably with chemical analysis obtained by EDX analysis. Annealed boron-doped samples lead to random crystallite orientations with predominantly (111) and (110) planes.

d) Stresses in as-grown films were as low as 18 MPa tensile for 20% Ge concentration. For similar Ge% concentration, thicker films tend to have less compressive stress. Stress for as-grown films tends to increase with Ge concentration. Annealed samples have tensile stress as low as 150 MPa. Tensile stress increases with anneal temperature. Samples annealed at greater than 700ºC or more than 20 hours at lower temperatures result in the film peeling off the substrate.

e) Hydrogen in the sample is bonded to Si and Ge. The Si-H stretching mode is at $2000cm^{-1}$ while the Ge-H stretch mode is at 1950 cm^{-1}. Hydrogen is more selectively bonded with Si than with Ge. The absence of wagging modes points to presence of less hydrogen in the sample due to high deposition temperatures. Annealing of the samples results in hydrogen effusion from the sample confirmed by absence of stretching modes in the sample.

f) As-grown samples have aggregate grain sizes varying from 20nm to 500nm. The larger grains are clusters of smaller grains. Annealing the sample leads to redistribution of the grains and their sizes vary from 20nm to 200nm.

g) Resistivity for as-grown boron doped samples was as-low as 1.3 m? -cm with annealed samples also having similar resistivity values. Phosphorous doped as-grown samples had higher resistivity values of about 5 ? -cm and annealed samples gave lower resistivities of about 5m? -cm.

h) Increase in Ge concentration and deposition temperature resulted in lower resistivity values. Increase in anneal temperature also resulted in lower resistivity values with dopant activation around 575ºC in phosphorous doped samples.

i) Photothermal Deflection Spectroscopy (PDS) gave the optical bandgap of the alloy at 20% Germanium concentration to be 1.6 eV. Annealing the sample resulted in increased absorption, probably due to free carrier absorption.

Building upon the characterization of boron and phosphorous doped layers, Hetero-junction bipolar (HBT) transistors can be fabricated. By employing Si/SiGe hetreostructures for heterojuntion bipolar transistors (HBT), researchers have been able to achieve cut-off and maximum oscillation frequencies past 100 GHz [34, 35]. This doubled the frequency output of Si HBTs and has given a platform for Si based technologies to compete with III-V devices. SiGe technologies in the development stages for HBTs in bipolar CMOS devices include power amplifiers for cellphones, wireless local-area network, numerous other transmitters in the >1GHz range and low noise amplifiers in front-end receivers.

Bosch has successfully used poly SiGe as an encapsulating layer in their accelerometers. Thermal insulated bolometers are realized by micromachining the active element i.e. poly SiGe to form a microbridge anchored to the substrate through thin supports. The thermal insulation is determined by the geometry and thermal conductivity of the samples.

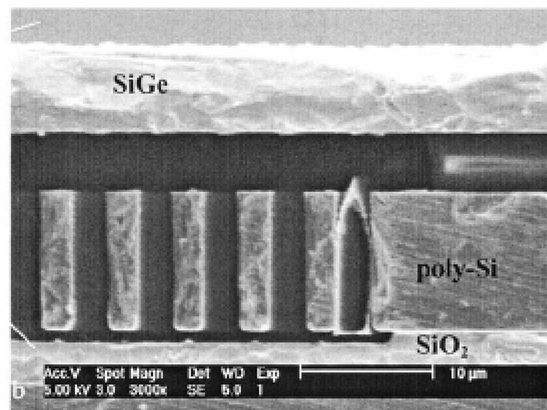

Fig 7.1 cross-section shows PECVD poly-SiGe as encapsulating layer above a Bosch accelerometer and HF etching of sacrificial SiO_2 [11].

8.0 APPENDIX

8.1 X-Ray Diffraction.

As Grown samples:
Sample: 050530

2Theta (2?)	**d spacing (Å)**	**$h^2+k^2+l^2$**	**Orientation**
27.3	3.27	2.8	111
47.4	1.99	7.5	220
53.7	1.7	10.4	311

Table 8.1 shows data for as grown sample doped with phosphorous

Sample :050422

2 Theta (2?)	**d spacing (Å)**	**$h^2+k^2+l^2$**	**Orientation**
28.1	3.15	3.04	111
46.8	1.93	8.1	220
55.6	1.65	11.1	311
75.6	1.25	19.3	331
87.1	1.11	24.5	422
105.2	0.96	32.7	440

Table 8.2 shows data for as grown sample doped with phosphorous

Sample : 050531

.

2 Theta (2?)	**d spacing (Å)**	**$h^2+k^2+l^2$**	**Orientation**
27.35	3.25	2.83	111
45.5	1.99	7.6	220
53.9	1.7	10.45	311

Table 8.3 shows data for as grown sample doped with phosphorous.

Sample: 050601

2Theta (2?)	d spacing (Å)	$h^2+k^2+l^2$	Orientation
27.35	3.25	2.83	111
45.5	1.99	7.6	220
53.85	1.7	10.45	311

Table 8.4 shows data for as grown sample doped with phosphorous.

Sample: 050318.

2Theta (2?)	d spacing (Å)	$h^2+k^2+l^2$	Orientation
27.4	3.25	2.83	111
45.6	1.99	7.6	220
54	1.7	10.45	311

Table 8.5 showing data for as grown sample doped with boron

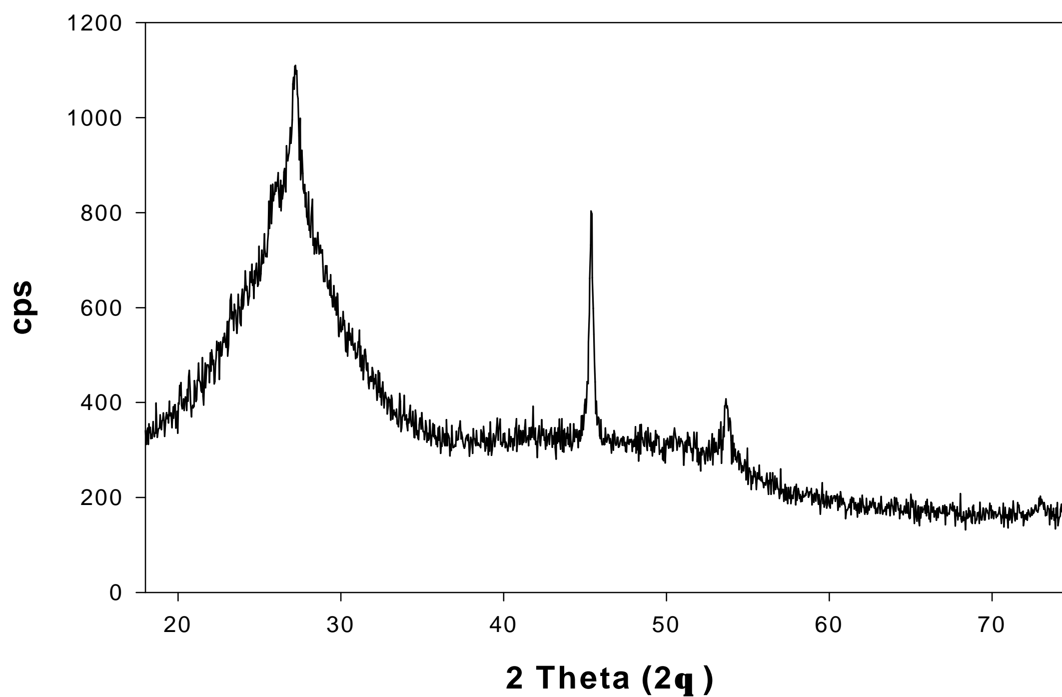

Figure 8.1 shows x-ray peaks for as-grown sample doped with phosphorous.

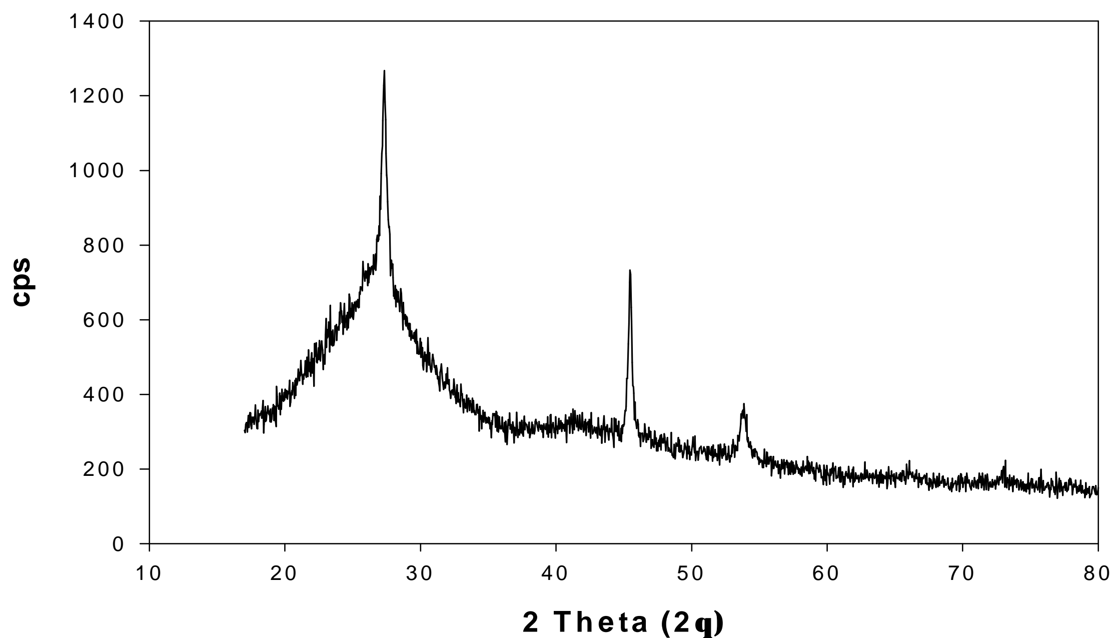

Figure 8.2 shows x-ray peaks for as-grown sample doped with phosphorous.

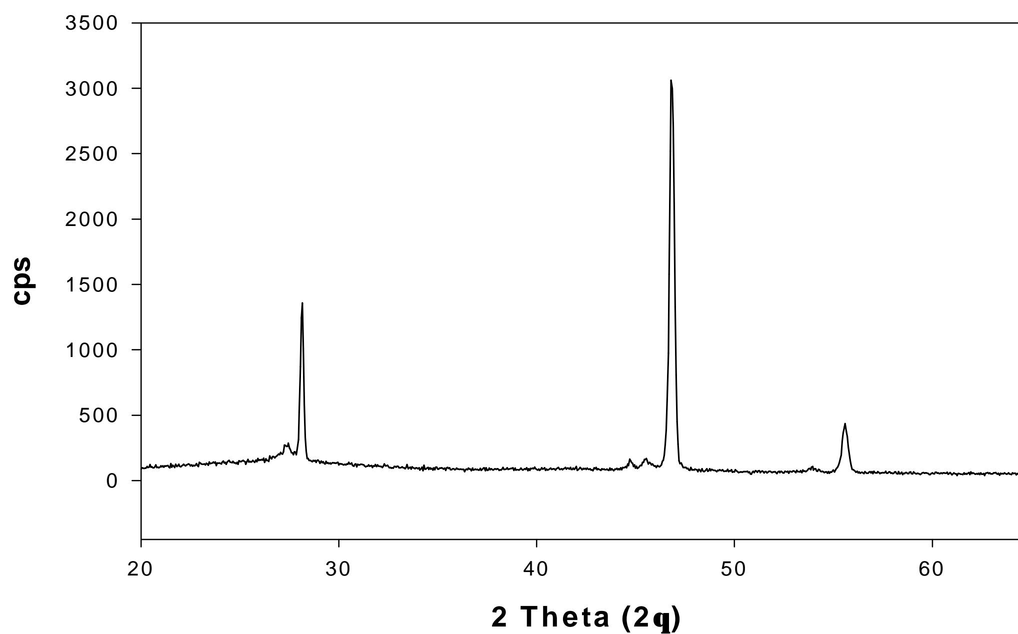

Figure 8.3 shows x-ray peaks for as-grown sample doped with phosphorous.

X-Ray Diffraction : 050422

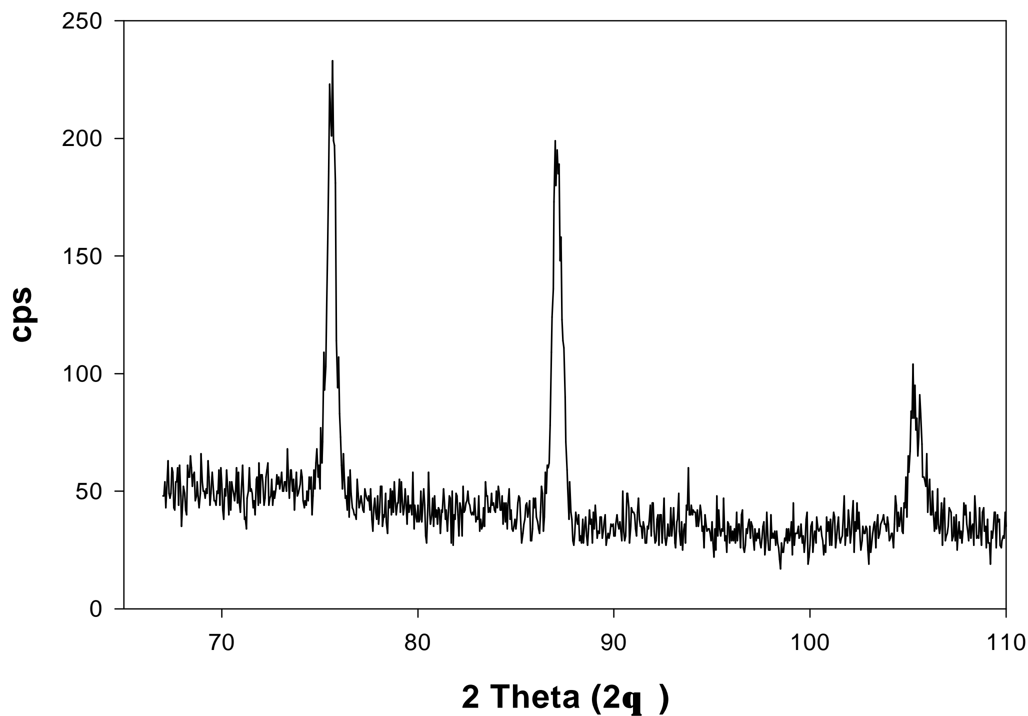

Figure 8.4 shows x-ray peaks for as-grown sample doped with phosphorous.

X-Ray Diffraction

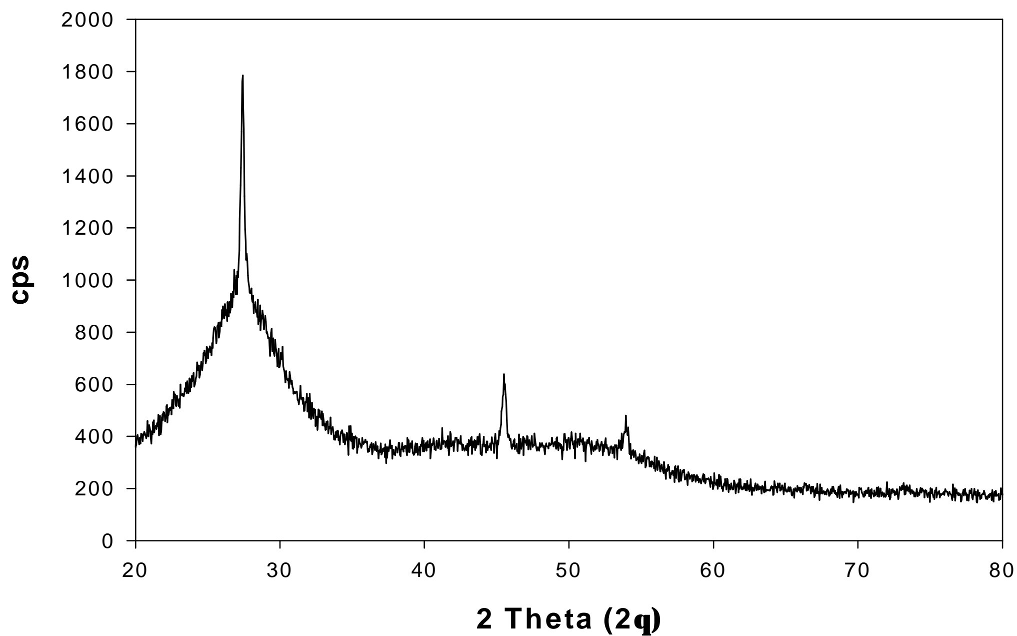

Figure 8.5 shows x-ray peaks for as-grown sample doped with boron.

Annealed Samples:

Sample: 050530.

2Theta (2?)	**d spacing (Å)**	**$h^2+k^2+l^2$**	**Orientation**
27.5	3.24	2.85	111
28.1	3.17	2.97	111
45.7	1.98	7.63	220
46.7	1.94	7.95	220
54.25	1.69	10.47	311
55.4	1.65	11	311
73.55	1.29	18	331
75.2	1.26	18.84	331

Table 8.6 shows data for annealed sample doped with phosphorous.

Sample: 050601.

2Theta (2?)	**d spacing (Å)**	**$h^2+k^2+l^2$**	**Orientation**
27.4	3.25	2.83	111
28.2	3.16	3	111
45.5	1.99	7.55	220
46.9	1.94	7.95	220
53.95	1.7	10.4	311
55.6	1.65	11	311
73.1	1.29	18	331
75.65	1.26	18.84	331

Table 8.7 shows data for annealed sample doped with phosphorous.

Sample: 050318.

2Theta (2?)	**d spacing (Å)**	**$h^2+k^2+l^2$**	**Orientation**
27.45	3.25	2.83	111
28.3	3.15	3	111
45.5	1.99	7.55	220
47.1	1.93	8	220
54.0	1.7	10.35	311
55.9	1.65	11	311
68.9	1.36	16	400
76	1.25	19.1	331

Table 8.8 shows data for annealed sample doped with boron.

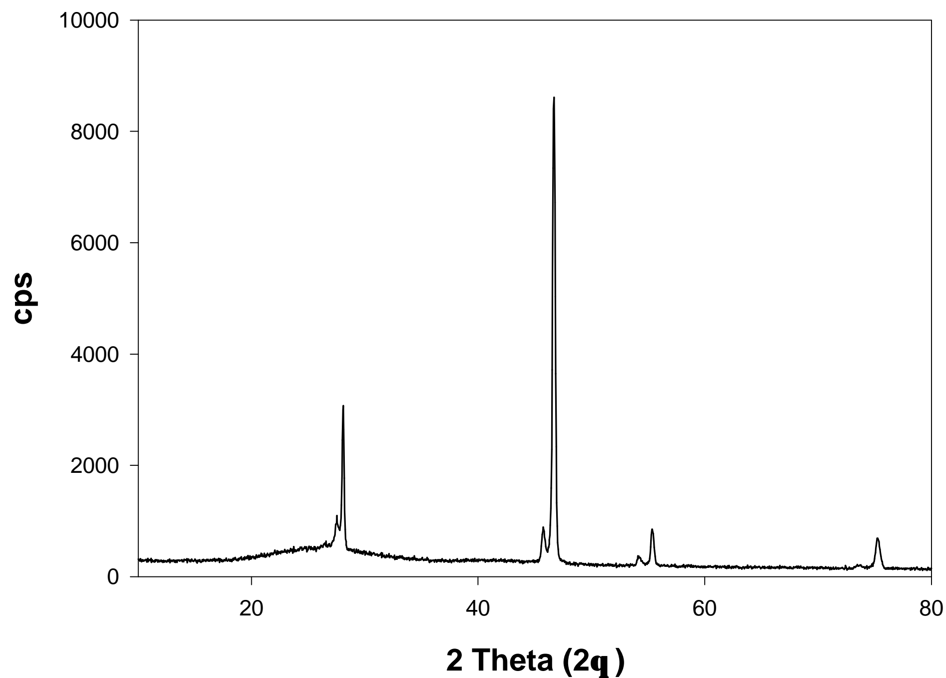

Figure 8.6 shows x-ray peaks for annealed samples doped with phosphorous.

X-Ray Diffraction

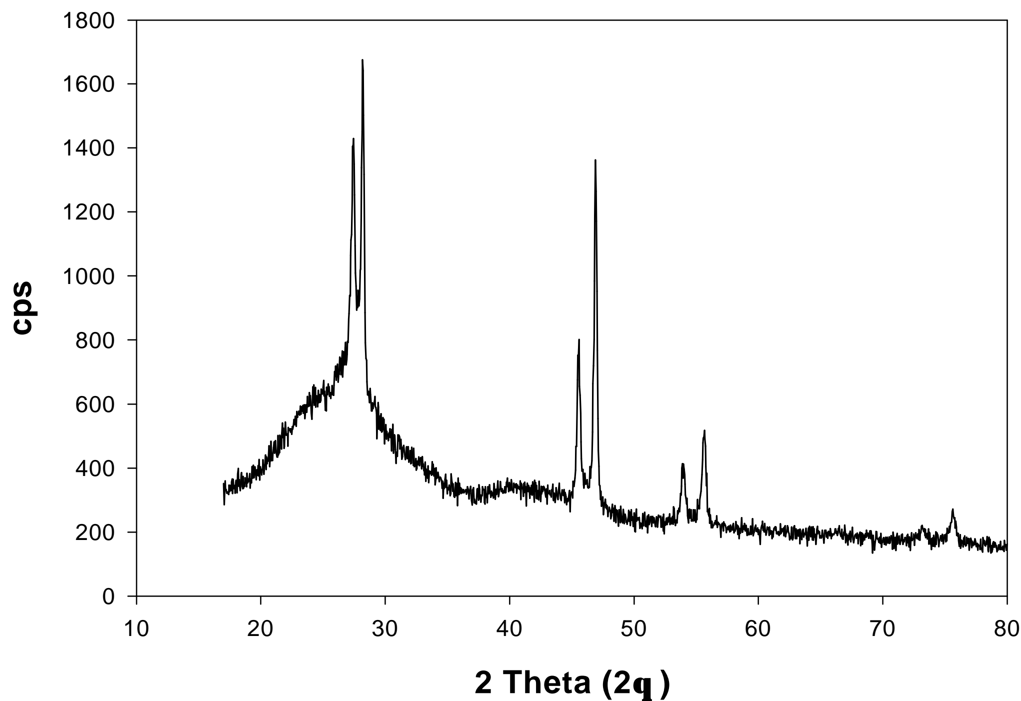

Figure 8.7 shows x-ray peaks for annealed samples doped with phosphorous.

X-Ray Diffraction : Annealed(050318)

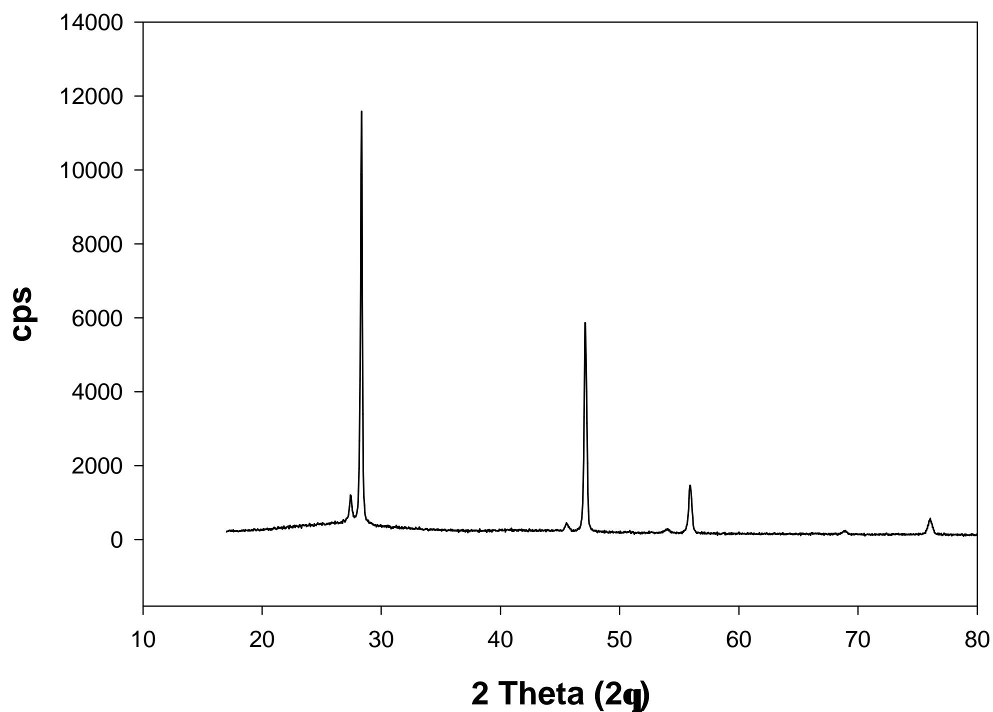

Figure 8.8 shows x-ray peaks for annealed samples doped with boron.

8.2 Stress Curves:

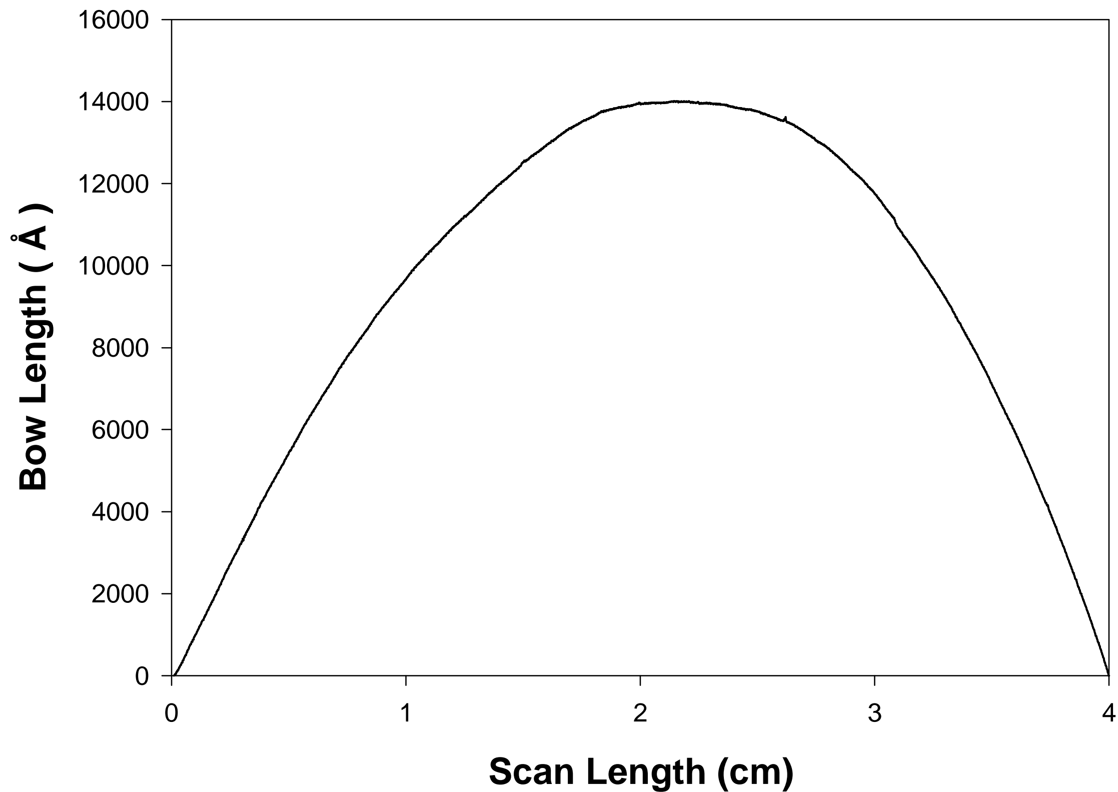

Figure 8.9 shows curvature of substrate measured by profilmetry.

Radius of Curvature (R) = L^2 / 8B.

L = Scan length = 4cm.

B = Bow Length of the film = 1.4 μm.

R = 142.85 m.

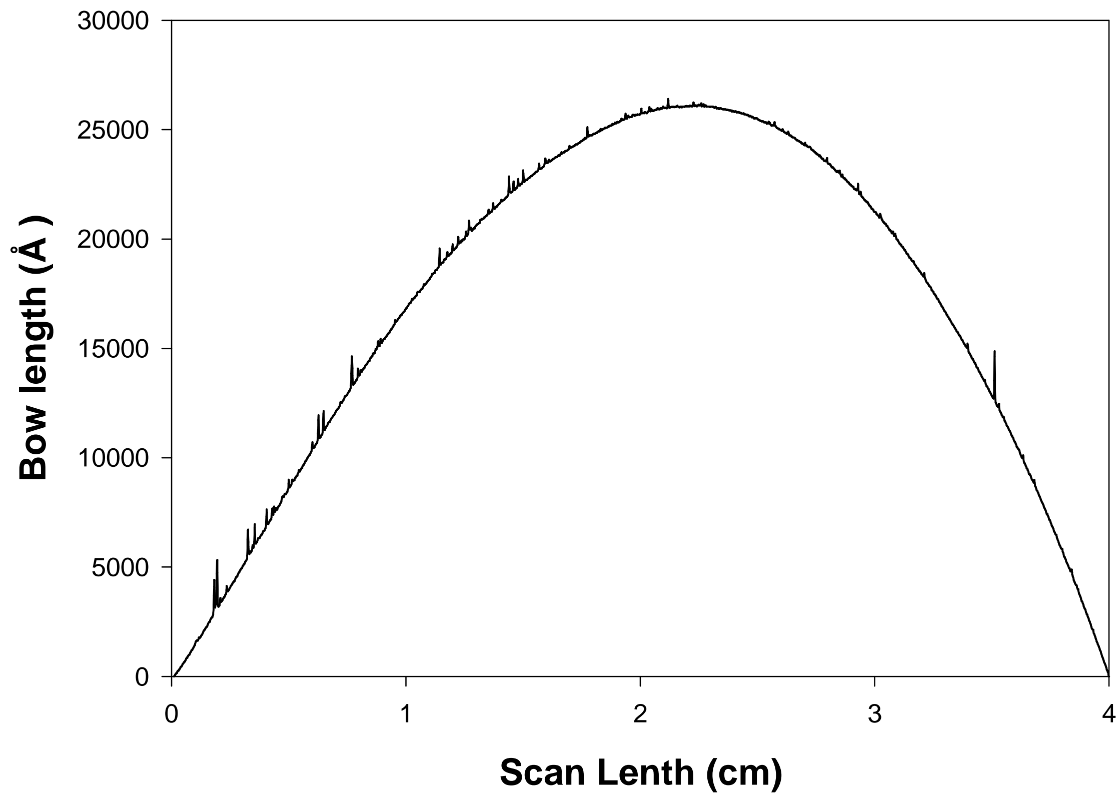

Figure 8.10 shows curvature of as grown film as measured by profilmetry.

Radius of Curvature (R) = $L^2 / 8B$.
L = Scan length = 4cm.
B = Bow Length of the film = 2.6 μm.
R = 83.33 m

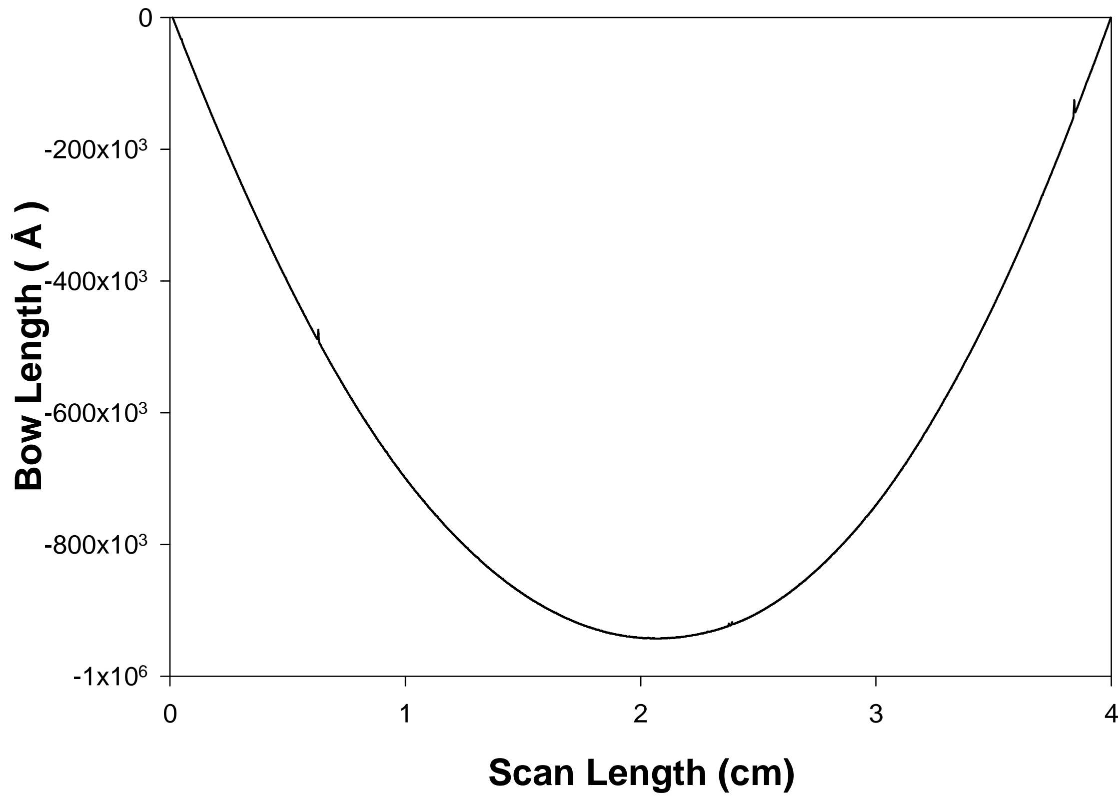

Figure 8.11 shows curvature of annealed film as measured by profilmetry.

Radius of Curvature (R) = $L^2 / 8B$.
L = Scan length = 4cm.
B = Bow Length of the film = 94 µm.
R = 14.92 m.

8.3 Properties of SiGe, Ge and Si.

Properties	Ge	$Si_{.25}Ge_{.75}$	$Si_{.5}Ge_{.5}$	$Si_{.75}Ge_{.25}$	Si
Atoms/cm^3	4.42×10^{22} Ge	4.415×10^{22}	4.61×10^{22}	4.805×10^{22}	5.0×10^{22}
Atomic weight	72.60 Ge	61.4725	50.345	39.2175	28.09 Si
Breakdown field (V/cm)	$\sim 10^5$ Ge	1.5×10^5	2×10^5	2.5×10^5	$\sim 3 \times 10^5$ Si
Crystal Structure	Diamond	Diamond	Diamond	Diamond	Diamond
Density (g/cm^3)	5.3267 Ge	4.577	3.827	3.078	2.328 Si
Dielectric constant	16.0 Ge	4.975	13.95	12.925	11.9 Si
Effective density of States in conduction band, N_c (cm^{-3})	1.04×10^{19} Ge				2.8×10^{19} Si
Effective density of States in valence band, N_v (cm^{-3})	6.0×10^{18} Ge				1.04×10^{19} Si
Effective Mass, m^*/m_0 Electrons Holes	$m^*_l = 1.64$ $m^*_t = 0.082$ $m^*_{lh} = 0.044$ $m^*_{hh} = 0.28$ Ge				$m^*_l = 0.98$ $m^*_t = 0.19$ $m^*_{lh} = 0.16$ $m^*_{hh} = 0.49$
Electron affinity X(V)	4.0	4.0125	4.025	4.0375	4.05
Minimum Indirect Energy Gap (eV) at 300K	0.66	0.804	0.945	1.05	1.12 Si
Minimum Direct Energy Gap (eV)	.7	1.6	2.5	3.1	3.4
Intrinsic carrier concentration (cm^{-3})	2.4×10^{13}	1.8×10^{13}	1.2×10^{13}	0.6×10^{13}	1.45×10^{10}
Intrinsic Debye length (μm)	0.68	6.51	12.34	18.17	24
Intrinsic resistivity (O-cm)	47	$.575 \times 10^5$	1.15×10^5	1.725×10^5	2.3×10^5
Lattice Constant (A)	5.6575	5.5960	5.5373	5.4825	5.4310

Linear coefficient of thermal expansion, ? *L*/*L*? *T* (°C^{-1})	5.8 x 10^{-6}	5.0 x 10^{-6}	4.2 x 10^{-6}	3.4 x 10^{-6}	2.6 x 10^{-6}
Melting point (°C)	937	1056.5	1176	1295.5	1415
Minority carrier lifetime (s)	10^{-3}	1.375 x 10^{-3}	1.75 x 10^{-3}	2.125 x 10^{-3}	2.5 x 10^{-3}
Mobility (drift) (cm^2/V-s)	3900(electron) 1900(hole)	3300(electron) 1537.5(hole)	7700(electron) 1175(hole)	2100(electron) 812.5(hole)	1500(electron) 450(hole)
Optical – phonon energy (eV)	0.037				0.063
Phonon mean free path ?$_0$(Å)	105				76 (electron) 55 (hole)
Specific heat (J/g-°C)	0.31	.4075	.505	.6025	0.7
Thermal conductivity at 300 K (W/cm-°C)	0.6	.11	.083	.085	1.5
Thermal diffusivity (cm^2/s)	0.36	0.495	.63	.765	0.9
Vapor pressure (Pa)	1 at 1330°C 10^{-6} at 760°C	1 at 1410°C 10^{-6} at 795	1 at 1490°C 10^{-6} at 830°C	1 at 1570°C 10^{-6} at865°C	1 at 1650°C 10^{-6} at 900°C

Table 8.9 Comparision of SiGe, Ge and Si properties [36].

LIST OF REEFRENCES

[1] Sherif Sedky,Ann Witvrouw,Annelies Saerens, Paul Van Houtte,Jef Poortmans and Kris Baert. J.Mater. Res. Vol 16, No 9, Sep (2001).

[2] Vivek Subramanian and Krishna C. Saraswat. IEEE Trans. On Electron Devices, Vol 45, No 8, August (1998.)

[3] D. J. Paul. Physics World. 13, 27 (2000).

[4] B. Y. Tsaur, J. C. C. Fan, and R. P. Gale. Appl. Phys. Lett. 38, 176 (1981).

[5] S. F. Fang, K. Adomi, S. Iyer, H. Morkoç, H. Zabel, C. Choi, and N. Otsuka. J. Appl. Phys. 68, R31 (1990).

[6] J. M. Kuo, E. A. Fitzgerald, Y. H. Xie, and P. L. Silverman. J. Vac. Sci. Tech. B. 11, 857 (1993).

[7] E. A. Fitzgerald, J. M. Kuo, Y. H. Xie, and P. L. Silverman. Appl. Phys. Lett. 64, 733 (1994).

[8] http://www.three-fives.com/latest_features/webzine_features/FinalSiGe.html

[9] R. Szweda. Adv. Semicond. Mag. 16, 36 (2003).

[10] O. Esame, Y. Gurbur, I. Tekin, and A. Bozkurt. Microelectronics Journal. 35, 901 (2004).

[11] Cristina Rusu, Sherif Sedky,Brigette Parmentier Journal of Microelectromechanical Systems, Vol 12, No 6, December (2003.)

[12] T. B. Massalski. Binary Alloy Phase Diagrams: GeSi. Am. Soc. for Met. 1-3 (Metal Park: New York) (1986).

[13] J. P. Dismukes, L. Ekstrom, and R. J. Paff. J. Phys. Chem. 68, 3021 (1964).

[14] D. V. Lang, R. People, J. C. Bean, and A. M Sergent. Appl. Phys. Lett. 47, 1333 (1985).

[15] Sherif Sedky,Paolo Fiorini, Kris Baert,Lou Hermans and Robert Mertens IEEE Trans. On Electron Devices, Vol 46, No 4, Apr (1999)

[16] David.S.Bang, Min Cao,Albert wang and Krishna.C.Saraswat Appl. Phys. Lett., Vol. 66, No. 2, 9 January (1995)

[17] Sherif Sedky, Kris Baert,Chris Van Hoof,Yi Wang,Omer Van derBiest and Ann Witvrouw. Mat.Res.Soc.Symp.Proc. Vol. 808 (2004)

[18] Sherif Sedky,Jeremy Schroeder,Timothy Sands, Roger Howe and Tsu-Jae King. Mat.Res.Soc.Symp. Vol. 741 (2003)

[19] W,Qin, D.G.Ast and T.I. Kamins. Mat.Res.Soc.Symp.Proc. Vol. 609 (2000)

[20] Sherif Sedky. Mat.Res.Soc.Symp.Proc. Vol.729 (2002)

[21] Sherif sedky, Ann Witvrouw and Matty Caymax, Amelies Saerens and Paul Van Houtte. J.Mater.Res, Vol. 17, Jul (2002)

[22] A.D. Compaan, X. Deng, and R.G. Bohn,Technical report, NREL (2001)

[23] Pratima Agarwal,H. Povolny ,S. Han X. Deng Journal of Non crystalline solids. 299-302 (2002)

[24] "Scanning Electron Microscopy and X-Ray Microanalysis" by Joseph, I. Goldstein, Dale E. Newbury, Patrick Echlin,David C. Joy, A.D. Romig, Jr., Charles E. Lyman, Charles Fiori, and Eric Lifshin. 2nd Edition,Plenum Press, (1992)

[25] "Basics of X-Ray Diffraction". Scintag Inc.p 7.5

[26] "Thin film stress measurement using profilometry": Mike Zeechino, Tim Cunningham

[27] Berkeley Microlab: Four point probe. J.Chang, (2004)

[28] University of Utah: Microfab: Four point probe manual (2003)

[29] Jacques I. Pankove Semiconductors and Semimetals. Hydrogenated amorphous silicon. Vol 21. Part B:Optical properties (1984)

[30] Stephen E. Bialkowski Volume 134 Chemical Analysis: A Series of Monographs on Analytical Chemistry and Its Applications. John Wiley & Sons, Inc (1996)

[31] Yu-Pin Chou and Si-Chen Lee Journal Of Applied Physics. Vol83, No 8 15 Apr (1998)

[32] G.Conte, D. Della Salle, F Galluzzi, G Grillo, C Ostrifate and C Reita Semicon.Sci.Tech. 5(1990) 890-893.

[33] Yoshimine Kato, Y. Kaida, Y. Miyoshi, and M. Atsumi 39th Electronic Materials Conference

[34] E. Crabbé. IEEE Tech. Digest 51$_{st}$ Device Research Conf. (New York) (1993).

[35] A. Schüppen, A. Gruhle, H. Kibbel, U. Erben, and U. König. IDEM Tech. Digest. (IEEE: New York) 377 (1994).

[36] Virginia Semiconductor.

[37] K.Kuwahara , Thin Solid Films, 78 (1981),pp 41-47.

[38] Sherif Sedky, Paolo Fiorini, Matty Caymax, Agnes Verbist, Chris Baert. Sensors and Actuators A 66 (1998) 193-199.

[39] G.D. Cody, T.Tiedje, B.Abeles,B.Brooks and Y.Goldstein. Physics review letter. Vol 47. No 20 (1981)

[40] V.I Kuzntsov,M.Zeman,L.L.A Vosteen,B.S. Girwar and J.M. Metselaar. J.Appl.Phys. 80 (11) December (1996).

[41] Wai Lo,a,z Hong Lin,a Wei-Jen Hsia,a Colin Yates,a Verne Hornback,a Jim Elmer Journal of the Electrochemical Society, 152 (1) G110-G114 (2005)

[42] http://www.chembio.uoguelph.ca/educmat/chm729/afm/details.htm